Pressure-induced superconductivity in CrAs and MnP

2017 J. Phys.: Condens. Matter 29 383003

(http://iopscience.iop.org/0953-8984/29/38/383003)

IOP Publishing Journal of Physics: Condensed Matter

J. Phys.: Condens. Matter **29** (2017) 383003 (27pp) https://doi.org/10.1088/1361-648X/aa7b01

Topical Review

Pressure-induced superconductivity in CrAs and MnP

Jinguang Cheng[1,3] **and Jianlin Luo**[1,2,3]

[1] Beijing National Laboratory for Condensed Matter Physics and Institute of Physics, Chinese Academy of Sciences, Beijing 100190, People's Republic of China
[2] Collaborative Innovation Center of Quantum Matter, Beijing, People's Republic of China
[3] School of Physical Sciences, University of Chinese Academy of Sciences, Beijing 100190, People's Republic of China

E-mail: jgcheng@iphy.ac.cn and jlluo@iphy.ac.cn

Received 20 June 2016, revised 24 March 2017
Accepted for publication 22 June 2017
Published 18 August 2017

Abstract

Transition-metal monopnictides, CrAs and MnP, were studied over 50 years ago due to the presence of interesting magnetic properties: CrAs forms a double-helical magnetic structure below $T_N \approx 270$ K accompanied by a strong first-order structural transition, while MnP first undergoes a ferromagnetic transition at $T_C \approx 290$ K and then adopts a similar double-helical order below $T_s \approx 50$ K. Both compounds are correlated metals and exhibit distinct anomalies at these characteristic magnetic transitions. By using high pressure as a clean tuning knob, we recently observed superconductivity with a maximum superconducting transition temperature of $T_c \approx 2$ K and 1 K when their helimagnetic orders are suppressed under a critical pressure of $P_c \approx 0.8$ and 8 GPa for CrAs and MnP, respectively. Despite a relatively low T_c, CrAs and MnP are respectively the first superconductor among the Cr- and Mn-based compounds in that the electronic density of states at the Fermi energy are dominated by Cr/Mn-3d electrons. These discoveries, in particular the close proximity of superconductivity to the helimagnetic order reminiscent of many unconventional superconducting systems, have attracted considerable attention in the community of superconductivity. The evolution of the helimagnetic order under pressure and its relationship with superconductivity have been actively investigated recently. Much effort has also been devoted to exploring more novel Cr- or Mn-based superconductors, leading to the discovery of quasi-1D $A_2Cr_3As_3$ (A = K, Rb, Cs) superconductors. In this review article, we will summarize the current progress achieved regarding superconductivity in CrAs and MnP.

Keywords: superconductivity, CrAs, MnP, high pressure

(Some figures may appear in colour only in the online journal)

1. Introduction

Superconductivity (SC), discovered a century ago, remains one of the most active research topics in modern condensed matter physics [1]. In particular, the discovery of several classes of unconventional superconducting systems, including heavy-fermion [2], high-T_c cuprate [3], and iron-based superconductors [4], has aroused tremendous research interest over the past three decades from the perspective of both fundamental research and practical applications. The latest discovery of iron-based superconductors in 2008 demonstrated that unconventional high-T_c SC is not limited to copper oxides, and other transition-metal compounds are also likely to give rise to new classes of superconductors that await our discovery [5]. As a matter of fact, SC has been observed in the majority of 3d transition-metal-based compounds except for the Cr- and

Mn-based ones, which are commonly antagonistic to SC due to the strong magnetism. For example, although SC can be readily achieved in $BaFe_2As_2$ when the Fe is partially replaced by Co or Ni [6], substitutions of Mn or Cr for Fe cannot induce SC [7, 8]. It is thus of great interest to explore possible SC in Cr- and Mn-based compounds [9, 10].

Although static magnetism is usually incompatible with SC, the short-range magnetic fluctuations have been considered as an essential ingredient for mediating Cooper pairs in the unconventional superconducting systems in which SC usually emerges in the vicinity of a long-range magnetically ordered state [11–13]. Therefore, the destabilization of the static magnetic order via either chemical doping or the application of external pressure provides an important guideline to search for new classes of unconventional superconductors. Alternatively, realizing a magnetic quantum critical point (QCP) is regarded as a key point in this direction [14, 15].

By following such an approach, we recently observed SC in the transition-metal monopnictides, CrAs and MnP, via the application of external pressure [16, 17]. These two compounds have been extensively studied for over 50 years due to the observations of interesting magnetic properties: CrAs forms a double-helical magnetic structure below $T_N \approx 270\,K$ accompanied by a strong first-order structural transition [18, 19], while MnP first undergoes a ferromagnetic (FM) transition at $T_C \approx 290\,K$ before adopting a similar double-helical order below $T_s \approx 50\,K$ [20–23]. We found that these two compounds become superconducting with a maximum $T_c \approx 2\,K$ for CrAs and $T_c \approx 1\,K$ for MnP when their long-range magnetic orders are suppressed at a critical pressure of $P_c \approx 0.8\,GPa$ and 8 GPa, respectively [16, 17].

Despite a relatively low T_c for both compounds, they are respectively the first superconductor among the Cr- and Mn-based compounds, and these discoveries have thus stimulated considerable research interest in the community of SC. A number of follow-up experiments, including neutron diffraction [24–26], nuclear magnetic/quadrupole resonance (NMR/NQR) [27, 28], muon spin rotation (μSR) [29, 30], magnetic x-ray diffraction (XRD) [31] under high pressures, as well as infrared optical spectroscopy [32] have been performed on CrAs and/or MnP to investigate the mechanism of observed SC. First-principles calculations have also been carried out to elucidate the unusual evolution of the magnetic ground states in MnP [33]. Both NMR/NQR and neutron scattering experiments for CrAs under pressure have shown the presence of strong magnetic fluctuations that may play an important role for the superconducting pairing mechanism [25, 27]. In addition, like Sr_2RuO_4 [34], UGe_2 [35], and some other heavy fermions [11], the superconducting volume and the transition temperature of CrAs were found to be very sensitive to the sample purity [16]. Moreover, typical behaviors associated with the antiferromagnetic (AF) quantum criticality, such as the non-Fermi-liquid (nFL) behavior and the dramatic enhancement of the effective electronic mass, were also observed near P_c for both CrAs and MnP, implying that the critical spin fluctuations might play an important role for the observed SC [16, 17, 36]. All these properties suggest a possible unconventional pairing mechanism for both compounds. As pointed out by Norman [37], it provides an excellent opportunity to study the interplay between unconventional SC and helimagnetism (HM) which has been rarely studied in the known superconducting systems. Furthermore, these discoveries have opened up a new avenue for exploring novel superconductors in the Cr- and Mn-based 3d transitional-metal compounds, as exemplified by the recent discoveries of the quasi-1D superconductors $A_2Cr_3As_3$ (A = K, Rb, Cs) [38–40].

Considering the growing interest and rapid accumulation of the experiment results in this field, we provide here a brief review on the recent progress of the pressure-induced SC in CrAs and MnP. For each section on CrAs and MnP below, we first overview their structural and physical properties at ambient pressure, present the discovery of pressure-induced SC, and then summarize the recent follow-up studies. We will conclude with a short summary and perspectives on future research directions.

2. CrAs

2.1. Structure and physical properties of CrAs at ambient pressure

2.1.1. Crystal structure of CrAs. Both CrAs and MnP crystallize in the orthorhombic B31 structure, which, often referred to as the MnP-type structure, is derived from the ideal hexagonal NiAs-type ($B8_1$) structure via the displacement of atoms. Figure 1 illustrates the relationship between these two types of structures, whose unit-cell parameters are related to each other via $a \approx c_h$, $b \approx a_h$, and $c \approx \sqrt{3}a_h$ (see chapter 1 of [41] for a detailed description). Note, the orthorhombic unit cell is defined in the *Pnma* space group with $c > a > b$. In the NiAs-type structure (figure 1(a)), the transition-metal atoms form a simple hexagonal lattice and the pnicogen anions form a lattice of a hexagonal closed-packed structure. The orthorhombic distortion of the MnP-type structure from the NiAs-type structure can be characterized by five crystallographic parameters: [41] δ, u, ε, v, w: the orthorhombic distortion is characterized by $\delta \equiv \left(c - \sqrt{3}b\right)/\sqrt{3}b$, while the position displacements along the orthorhombic c and a axis are uc and εa for the transition-metal atoms, and va and wc for the pnicogen atoms, respectively. All these parameters become zero for the NiAs-type structure. Table 1 lists these parameters for the orthorhombic CrAs and MnP [41]. Since ε and w are about one order of magnitude smaller than u and v, the major displacements of the transition-metal and pnicogen atoms take place along the orthorhombic c and a axis, respectively, as indicated by the arrows in figure 1(b).

At ambient conditions, the lattice parameters of CrAs are $a = 5.650$ Å, $b = 3.463$ Å, and $c = 6.205$ Å, respectively. It has been reported that CrAs has a structural phase transition from the orthorhombic MnP type to the hexagonal NiAs type above 1100 K [42]. Below room temperature, CrAs undergoes an isostructural phase transition accompanying the magnetic order at $T_N \approx 270\,K$, as detailed below.

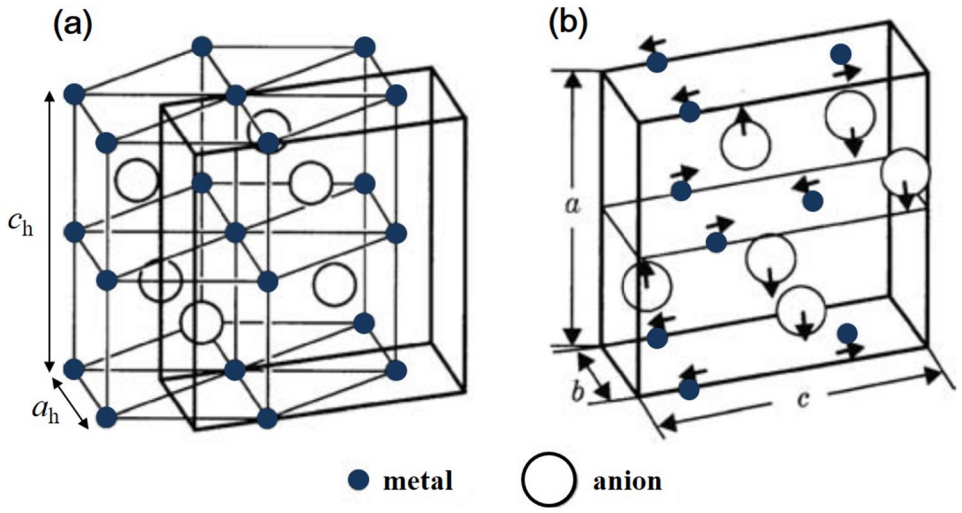

Figure 1. The relation between the hexagonal NiAs-type and orthorhombic MnP-type crystal structure. (a) The NiAs-type structure. The thick lines denote the unit cell corresponding to the MnP-type structure. (b) The unit cell of the MnP-type structure with the arrows indicating the displacements of atoms. The small solid circles represent the metal atoms, and the large open circles represent the anions. [41] 2009 Springer-Verlag Berlin Heidelberg. With permission of Springer.

2.1.2. Magnetic properties of CrAs. The magnetic and structural properties of polycrystalline CrAs below room temperature have been extensively studied for decades by means of neutron and XRD, magnetic susceptibility, specific heat, and transport measurements [18, 19, 24, 43, 44]. The neutron diffraction experiments revealed that CrAs is magnetically ordered below $T_N = 270$ K and its magnetic structure is double helical, as illustrated in figure 2. The spin vectors of the Cr moment of $1.73\mu_B$ lie and rotate within the *ab* plane, and the spiral propagates along the orthorhombic *c* axis with the propagation vector $\mathbf{q} = 0.356 \times 2\pi c^*$, where c^* denotes the vector in reciprocal space [18, 24, 43]. The angle between the spin vectors of the Cr atoms 2 and 3 is ~180°, which means that the dominant exchange interactions between spins on the corresponding atoms are AF. The spins on atoms 1 and 2 show a non-collinear arrangement with an angle of ~114°.

The double-helical magnetic transition at T_N was found to be a strong first order transition accompanied by discontinuous changes of lattice parameters [45]. The most dramatic change was a sudden expansion of lattice parameter *b* by ~4%, while the lattice parameters *a* and *c* shrank by <1% below T_N.

The magnetic susceptibility $\chi(T)$ of CrAs increases with temperature up to 1100 K, similar to that of the parent compounds of iron-based superconductors, which has been explained in terms of strong AF fluctuations [46]. On the other hand, $\chi(T)$ for the hexagonal phase at $T > 1100$ K was found to follow the Curie–Weiss behavior [42]. No anomaly at $T_N \approx 270$ K could be observed for the polycrystalline sample [18]. In contrast, the transition is well defined in the single crystal. In 2010, Wu *et al* successfully grew high-quality single crystals of CrAs by the tin (Sn) flux method [47]. Figure 3(a) shows the $\chi(T)$ for a needle-shaped CrAs single crystal with a magnetic field applied parallel and perpendicular to the longest dimension. The double helical transition at T_N is manifested as an abrupt change in $\chi(T)$ with considerable thermal hysteresis around T_N, in agreement with its first-order nature.

Table 1. The crystallographic parameters characterizing the orthorhombic distortions of CrAs and MnP (after [41]).

	δ	μ	ε	v	w
CrAs	0.036	0.05	0.007	0.05	0.006
MnP	0.077	0.05	0.005	0.06	0.01

2.1.3. Thermodynamic and transport properties of CrAs. Specific heat measurements for CrAs have been done by Kazama *et al* [48] and Barner *et al* [49]. A sharp peak around T_N was observed corresponding to the first-order magnetic transition. The latent heat found to be 5.3×10^2 J mol^{-1}. The electronic specific-heat coefficient γ obtained in the low-temperature range is 9.1 mJ (mol K^2)$^{-1}$. The resistivity $\rho(T)$ of the CrAs single crystal reported by Wu *et al* [47] is displayed in figure 3(b), which shows metallic temperature dependence with a sudden drop and pronounced thermal hysteresis at T_N. At low temperatures below 15 K, $\rho(T)$ follows a quadratic temperature dependence, i.e. $\rho(T) = \rho_0 + AT^2$. From the obtained coefficients A and γ, the Kadowaki–Woods ratio A/γ^2 of CrAs is estimated to be 1×10^{-5}, which is located nicely on the universal line for the correlated electron systems and is about one order larger than those of simple metals [47].

2.1.4. Effect of substitution on the magnetic transition. The intriguing first-order HM transition observed in CrAs was subjected to intense investigations with the aim of elucidating the intimate relationship between the structural and magnetic properties. Suzuki and Ido summarized the effect on T_N of the substitution of various transition metals for Cr or other pnicogen for As, and constructed a magnetic phase diagram in terms of T_N versus the *b*-axis length [50]. As shown in figure 4(a), for most substitution elements, T_N decreases rapidly with an increase in the composition *x*, except for the Mn and Sb-substituted samples. According to figure 4(b), there is a critical *b*-axis length, $b_c = 3.38$ Å; the helical magnetic

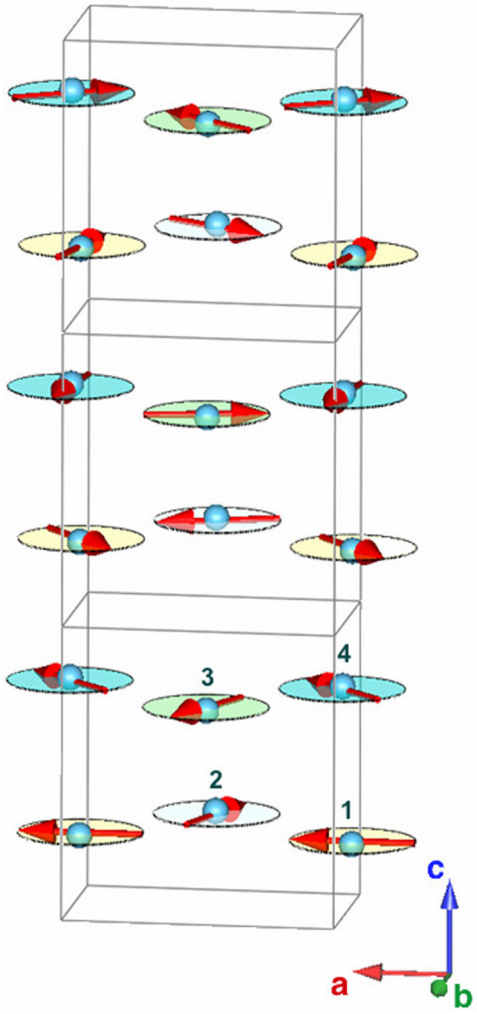

Figure 2. The incommensurate double helical magnetic structure of CrAs. The spin vectors lie in the *ab* plane, and the spiral propagates along the *c* axis with a propagation vector $\mathbf{q} = 0.356 \times 2\pi c^*$. The evolution of the moments is shown for a three-unit cell along the *c* axis. Reprinted figure with permission from [24], Copyright 2015 by the American Physical Society.

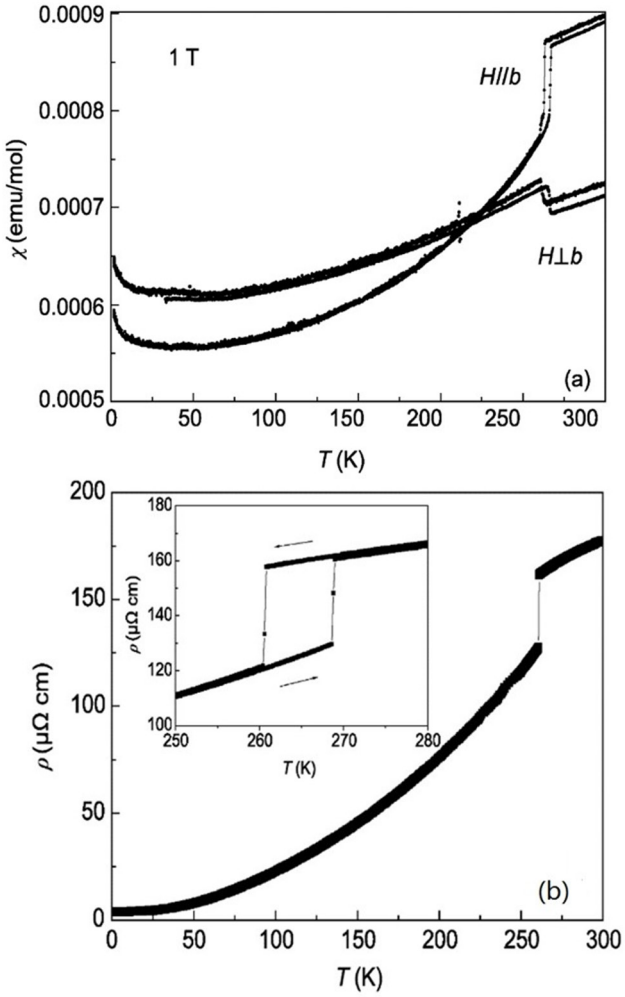

Figure 3. (a) Temperature dependence of magnetic susceptibility $\chi(T)$ measured upon thermal cycling under $H = 1$ T applied parallel and perpendicular to the longest dimension of the needle-shaped CrAs crystal. (b) Temperature dependence of resistivity $\rho(T)$ under zero field. The strong first-order nature of the double helical magnetic transition at T_N is manifested by the abrupt changes of both $\chi(T)$ and $\rho(T)$, as well as the thermal hysteresis shown in the inset of (b). Reprinted by permission from Macmillan Publishers Ltd: Nature Communications [16], Copyright 2014.

order exists only in the compounds with $b > b_c$, regardless of the substitution elements [50].

The effect of Mn substitution has been studied in more detail via x-ray and neutron diffraction, and magnetic susceptibility [43, 45, 51, 52]. Figure 5 depicts the phase diagram of $Cr_{1-x}Mn_xAs$ [43]. For $x < 0.5$, the compounds are helimagnetic with a MnP-type structure. Near $x = 0.6$, the compounds are FM at low temperatures, and undergo a phase transition to a helical order as the temperature increases. For $0.7 < x < 0.95$, the compounds show a metamagnetic behavior. The end member MnAs is FM with a high Curie temperature $T_C = 318$ K and experiences two NiAs–MnP–NiAs structural transformations upon cooling. The structural and magnetic properties of MnAs are also very interesting (see [41] for a review).

Unlike the substitutions on the Cr sites, partial replacements of As with smaller P or larger Sb only disturb the Cr sublattice to a minimal extent, yet can tune the magnetic and structural properties in distinct manners [44, 50, 53, 54]. The orthorhombic MnP-type structure can be maintained in the $CrAs_{1-x}P_x$ system, and the unit-cell parameters decrease with increasing x as expected. The application of chemical pressure via doping P reduces T_N quickly, which takes place at ~110 K for $x = 0.03$, and disappears completely around $x = 0.05$ [44]. In contrast, the application of negative chemical pressure via doping Sb induces changes in both the crystal and magnetic structures since the hexagonal NiAs-type CrSb adopts a simple collinear AF structure below $T_N = 718$ K. Suzuki and Ido have studied the crystallographic and magnetic properties of $CrAs_{1-x}Sb_x$ with $0 \leqslant x \leqslant 1$ by XRD and magnetic susceptibility experiments [54]. Figure 6 displays the $\chi(T)$ and the phase diagram for the system $CrAs_{1-x}Sb_x$. For $x \leqslant 0.5$, the NiAs-to-MnP type structural transition temperature T_t decreases monotonically, while the double helical transition T_N first increases, reaches a maximum around $x = 0.2$, and then decreases gradually until $x = 0.5$. T_t and T_N merge at $x \approx 0.4$. For $x > 0.5$, all compositions take a similar NiAs-type structure and a simple collinear AF order. T_N increases linearly from about 400 K for $x = 0.6$ K to 718 K for CrSb. For compositions $x = 0.6$ and

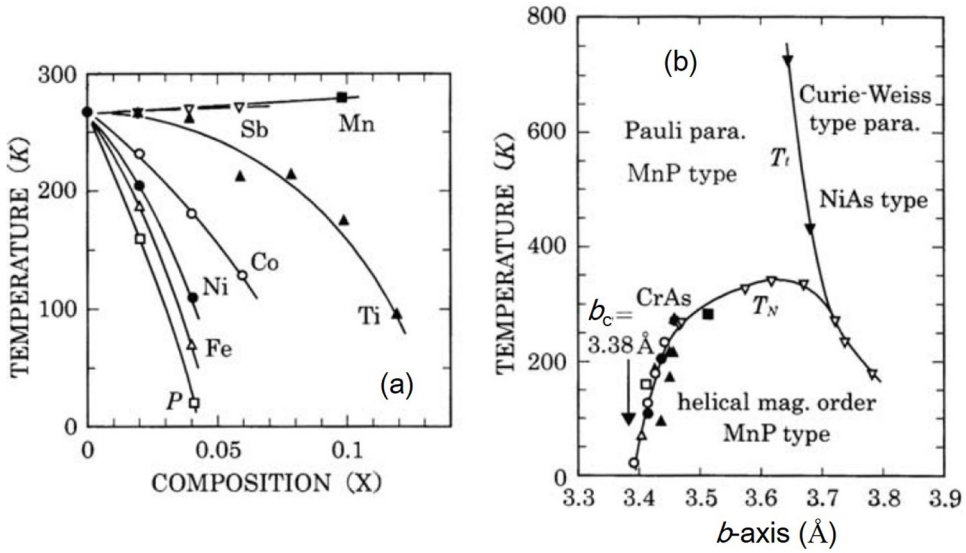

Figure 4. (a) Composition dependence of T_N for $Cr_{1-x}M_xAs$ (M = Ti (solid triangle), Mn (solid square), Fe (open triangle), Co (open circle), and Ni (solid circle)) and $CrAs_{1-x}Pn_x$ (Pn = P (open square), and Sb (inverted triangle)). Reprinted from [50], with the permission of AIP Publishing. (b) T_N of these compounds plotted as a function of *b*-axis length. T_t is the transition temperature of the NiAs–MnP structural transition. [41] 2009 Springer-Verlag Berlin Heidelberg. With permission of Springer.

0.7, another first-order structural transition exists at T_t', whose origin remains unclear. The ordered moments of Cr ions increase from 1.7 μ_B/Cr for CrAs to 3.0 μ_B/Cr for CrSb.

2.1.5. Effect of pressure on the magnetic transition. The effect of pressure on the magnetic transitions of CrAs and $CrAs_{1-x}Sb_x$ has been investigated by Zavadskii *et al* [55] and Yoshida *et al* [56]. Figure 7 shows $T_N(P)$ for $CrAs_{1-x}Sb_x$ with $0 \leqslant x \leqslant 0.36$. For CrAs, T_N decreases from about 260 K at ambient pressure to about 196 K at 0.38 GPa. The slope of T_N versus P for CrAs, dT_N/dP, is -160 K GPa^{-1}. Such a large pressure coefficient suggests that the magnetic transition temperature is very sensitive to external pressure. Zavadskii *et al* [55] showed that T_N of CrAs disappears at $P > 0.5$ GPa. For $CrAs_{1-x}Sb_x$ ($0.1 \leqslant x \leqslant 0.3$), dT_N/dP values are also negative, but the magnitude decreases as x increases.

2.2. Pressure-induced SC in CrAs

2.2.1. Discovery of SC in CrAs [16, 36]. As mentioned above, SC has been observed in the majority of 3d transition-metal compounds except for the Cr- or Mn-based ones. It is thus of great interest to explore possible SC in those systems. Previous studies on CrAs have demonstrated that the magnetism of Cr in CrAs is located very close to the boundary between localized and itinerant electron transition. The coupled structural, magnetic, and electronic degrees of freedom at T_N make external pressure an effective knob in fine tuning its properties [55, 56]. Motivated by the fact that unconventional SC frequently emerges on the border of magnetic order in heavy fermions, high-T_c cuprates and iron pnictides, we initiated a high-pressure study on the transport properties of CrAs crystal. Details have been published in [16]. We present below the essential high-pressure results.

Our measurements were performed on the needle-shaped CrAs single crystals grown with the Sn-flux method [47]. High-quality CrAs crystals with the residual resistivity ratio

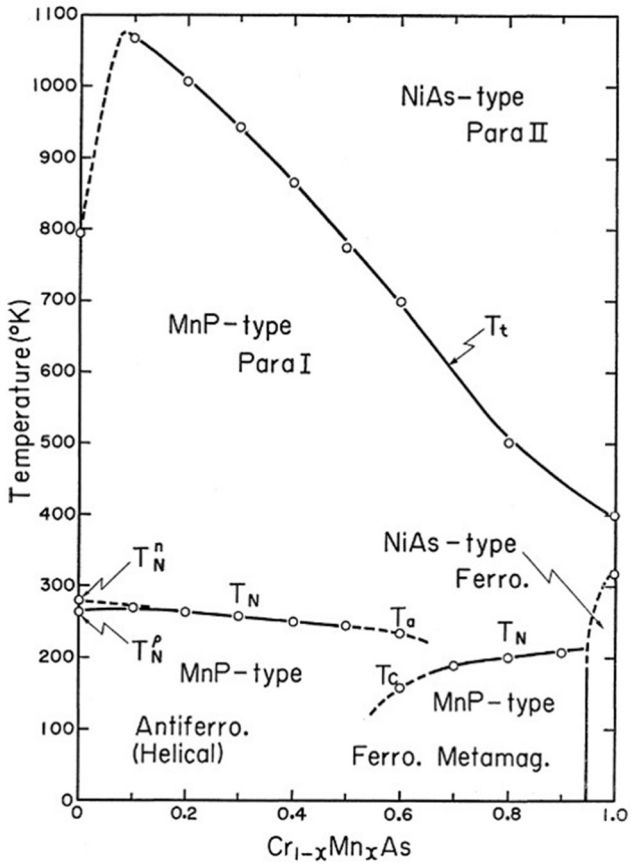

Figure 5. Magnetic phase diagram of the $Cr_{1-x}Mn_xAs$ system. T_N^n and T_N^ρ are helimagnetic transition temperatures obtained from NPD and resistivity measurements, respectively. Reprinted from [43], with the permission of AIP Publishing.

(RRR $\equiv R_{300\ K}/R_{5\ K}$) > 200 are essential in order to achieve zero-resistivity under pressure. Figure 8 displays the $\rho(T)$ under pressures up to 2.14 GPa for a representative sample. The first-order AF transition is manifested as a sudden drop of resistivity

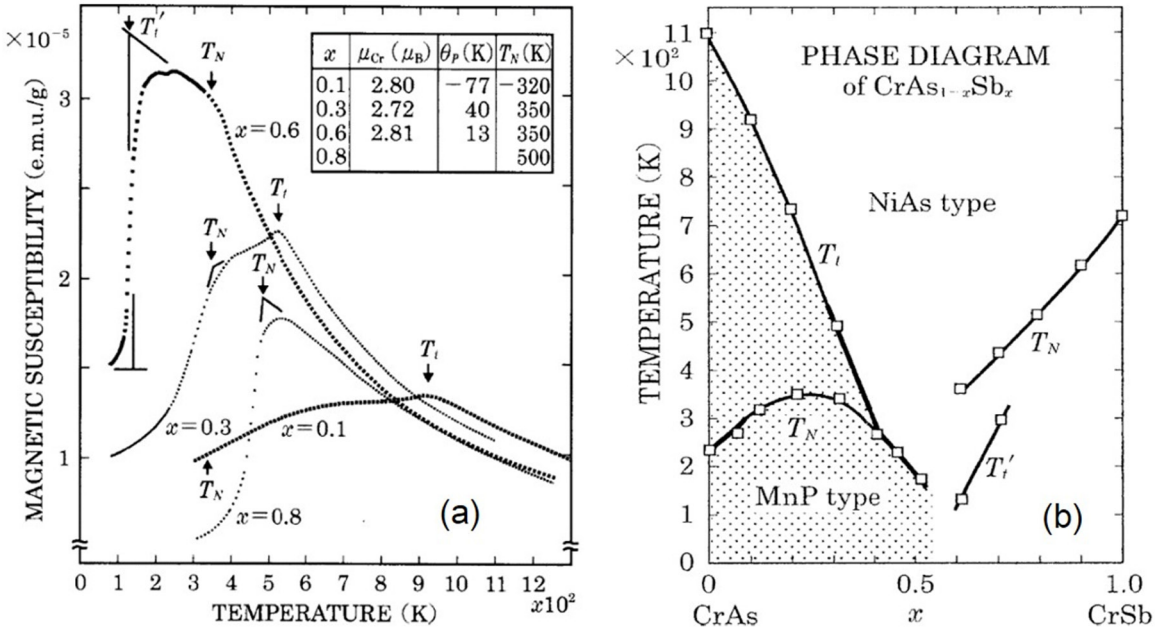

x	μ_{Cr} (μ_B)	θ_P (K)	T_N (K)
0.1	2.80	−77	−320
0.3	2.72	40	350
0.6	2.81	13	350
0.8			500

Figure 6. (a) Temperature dependence of magnetic susceptibility for $CrAs_{1-x}Sb_x$ with $x \leqslant 0.8$. T_N and T_t are transition temperatures of magnetic order and the NiAs-to-MnP type structural transformation. Reprinted from [54], with permission from Elsevier. (b) Phase diagram of CrAs–CrSb system. [41] 2009 Springer-Verlag Berlin Heidelberg. With permission of Springer.

at $T_N = 264$ K upon cooling at ambient pressure. The application of high pressure suppresses T_N progressively, and changes the resistivity anomaly at T_N from a sudden drop for $P < 0.3$ GPa to a smoothly-varied kink whose magnitude is also diminished gradually within the pressure range $0.3 < P \leqslant 0.7$ GPa. Such an evolution of the resistivity anomaly at T_N suggests a gradual crossover from strong to weak first-order transition, especially near the critical pressure where T_N vanishes. The resistivity anomaly disappears completely for $T > 3$ K and $P > 0.7$ GPa. The $\rho(T)$ data shown in figures 8(b) and (c) illustrate how the SC emerges and then evolves with pressure at low temperatures. At ambient pressure, SC is absent in CrAs down to 350 mK. With increasing pressure in the range $0.3 < P < 0.7$ GPa where T_N remains finite, the superconducting transition is featured by similar multi-step drops; the onset temperature first increases and then decreases with pressure, while the zero-resistivity temperature $T_c^0 \approx 1$ K keeps nearly constant. The multi-step feature disappears with a further increase in pressure, and finally changes to a single transition for $P > 0.8$ GPa where T_N vanishes completely, as seen in figure 8(c).

Ac susceptibility measurements were carried out to further verify the bulk nature of the observed SC in CrAs. As shown in figure 9, the diamagnetic signal starts to appear at $P > 0.3$ GPa, and the superconducting shielding fraction grows gradually with pressure, reaching over 90% of the sample volume above 0.8 GPa. The onset temperatures of the diamagnetic signal are also in excellent agreement with the $\rho(T)$ data shown in figure 8(c).

Kotegawa and co-workers in Kobe University independently studied the $\rho(T)$ of CrAs crystals under pressure and confirmed the pressure-induced SC [36]. It should be noted that the CrAs crystals used by Kotegawa *et al* exhibit a sharp jump in $\rho(T)$ below T_N at ambient pressure, different from that seen in [16, 47], where $\rho(T)$ shows an abrupt drop below T_N.

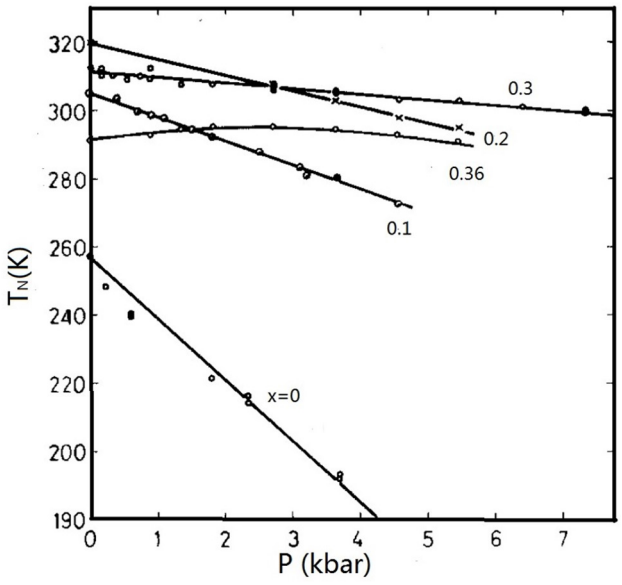

Figure 7. The pressure dependence of T_N for $CrAs_{1-x}Sb_x$ with $x = 0$, 0.1, 0.2, 0.3, and 0.36. Reprinted from [56], with permission from Elsevier.

As shown in figure 10(a), $\rho(T)$ does not return to its initial value after one thermal cycle, which is primarily attributed to the development of cracks in the crystal due to strong magnetostriction at the first-order transition. The critical pressure of $P_c = 0.7$ GPa is very close to that observed by Wu *et al* [16]. To avoid developing cracks, Kotegawa *et al* [36] applied pressure directly beyond P_c on the second CrAs crystal at room temperature so as to probe the superconducting transition shown in figure 10(b). SC with a maximum T_c of 2.17 K was observed under pressure of 10 kbar, slightly higher than that observed at the same pressure by Wu *et al* [16], presumably due to the

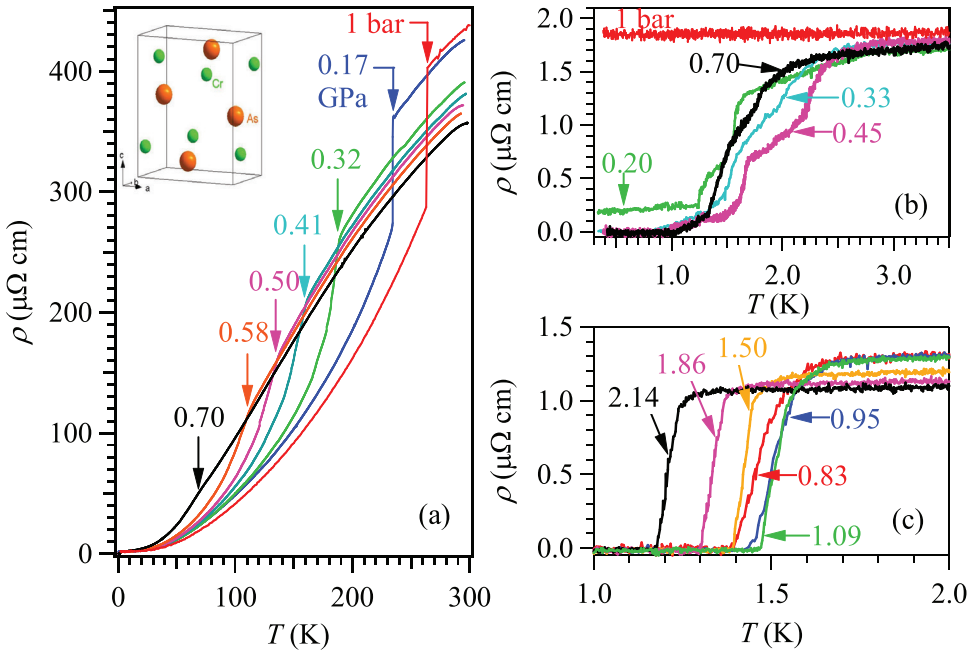

Figure 8. (a) Resistivity $\rho(T)$ of the CrAs single crystal under various hydrostatic pressures up to $P = 0.70$ GPa in the whole temperature range highlighting the variation with pressure of the antiferromagnetic transition temperature T_N indicated by arrows. $\rho(T)$ data at low temperatures for (b) $P \leqslant 0.7$ GPa with an inhomogeneous superconducting state, and (c) for $P \geqslant 0.83$ GPa with a single superconducting transition, highlighting the evolution with pressure of the superconducting transition. Reprinted by permission from Macmillan Publishers Ltd: Nature Communications [16], Copyright 2014.

elimination of cracks and/or strain similar to the post-annealing process in the Pr-doped $CaFe_2As_2$ superconductors [57].

2.2.2. T–P phase diagram and unconventional SC for CrAs. Figure 11(a) shows the *T–P* phase diagram of CrAs obtained by Wu *et al* [16]. As can be seen, the first-order AF transition temperature $T_N = 264$ K at ambient pressure can be suppressed quickly by pressure, and T_N approaches zero temperature at a critical pressure $P_c \approx 0.8$ GPa. At $P \geqslant P_c$, bulk SC with a shielding fraction over 90% is achieved accompanied by a dramatic decrease of the 10%–90% SC transition temperature width ΔT_c, as seen in figure 11(b). For $0.3\,\text{GPa} < P < P_c$, the superconducting state coexists with the AF state, and the volume fraction grows gradually at the expense of the other. A similar *T–P* phase diagram was also obtained by Kotegawa *et al* [36], but the two-phase coexistent region is missing because the pressure was applied directly to above 0.7 GPa in order to observe the SC.

The *T–P* phase diagram of CrAs shown in figure 11(a) resembles that of many unconventional superconducting systems, including the heavy fermions [11], high-T_c cuprates [58], and iron-pnictide superconductors [59]. As a universal phase diagram in these systems, SC emerges in the vicinity of a critical point where a high-temperature magnetically ordered state is suppressed by applying external tuning parameters, such as doping charge carrier, chemical or physical pressure. The proximity of SC to the long-range magnetic order lends strong support to the unconventional pairing mechanism via magnetic fluctuations.

Besides a similar phase diagram with many unconventional superconductors, several points in CrAs are also in favor of the possible unconventional SC. Firstly, the

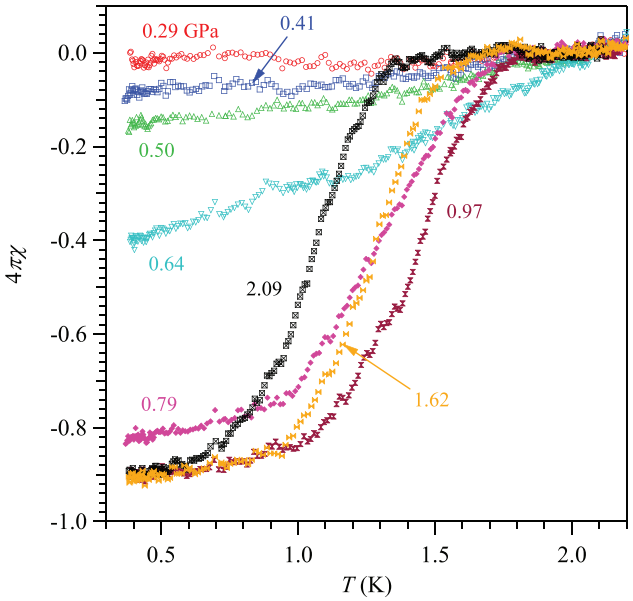

Figure 9. Temperature dependence of the ac magnetic susceptibility $4\pi\chi$ of a CrAs single crystal under various hydrostatic pressures. Reprinted by permission from Macmillan Publishers Ltd: Nature Communications [16], Copyright 2014.

normal-state resistivity $\rho(T)$ was found to follow a power-law $\rho(T) = \rho_0 + AT^n$ with $n = 1.5 \pm 0.1$ in a wide pressure range $0.3 < P < 2.1$ GPa where SC takes place, as shown in the inset of figure 11(a) [16]. The observed nFL exponent $n = 1.5 \pm 0.1$ is very close to the value predicated for incoherent scattering of quasiparticles via magnetic interactions in the 3D antiferromagnets [60, 61]. Secondly, the AF fluctuations actually seem to be abundant above T_N, since

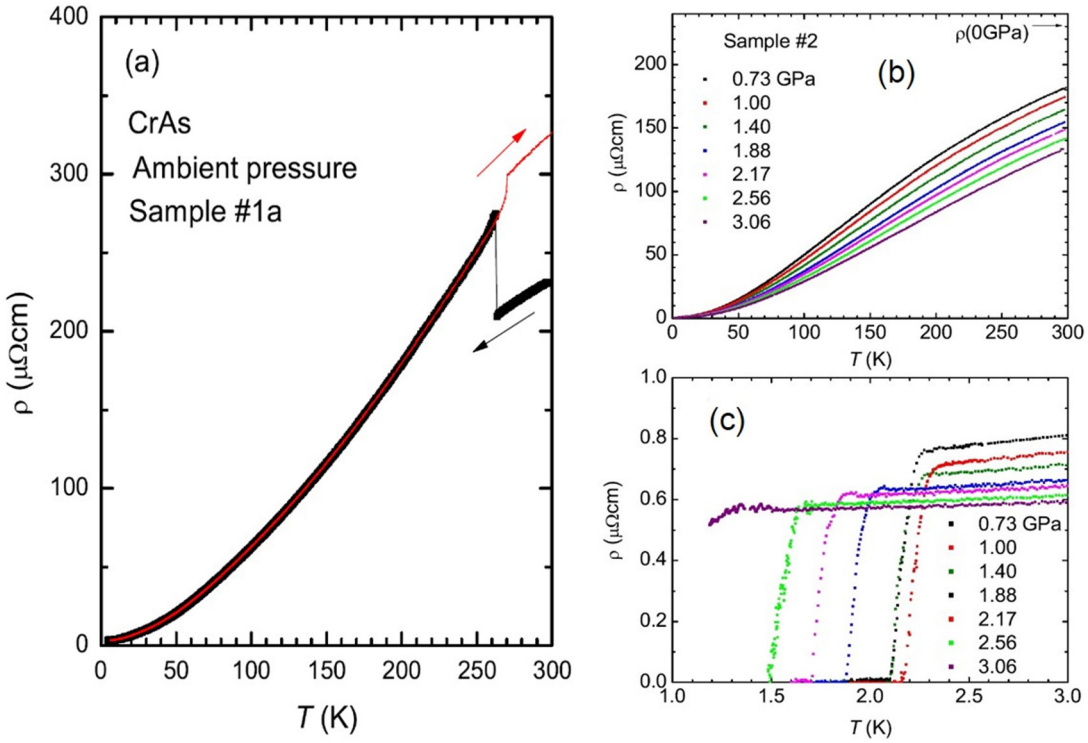

Figure 10. (a) Temperature dependence resistivity $\rho(T)$ of CrAs at ambient pressure from [36]. $\rho(T)$ shows a jump at T_N upon cooling. (b) $\rho(T)$ at different pressures in the paramagnetic phase. (c) $\rho(T)$ at low temperatures. Superconducting transition with a maximum T_c of 2.17 K at 1.0 GPa is shown. Reproduced with permission from [36].

the magnetic susceptibility of CrAs keeps increasing with temperature up to 1100 K at ambient pressure [56]. Such an increasing behavior of magnetic susceptibility has been found to be universal in the iron-based superconductors, and regarded as an indication of AF fluctuations [46]. In this regard, these spin fluctuations would be optimized near the critical pressure where the AF order of CrAs is suppressed completely. Finally, the pressure-induced SC is found to be very sensitive to sample purity. Wu *et al* found that only the high-quality CrAs crystals with RRR $>$ 200 showed bulk SC [16]. Although the CrAs crystals with RRR ~ 40–50 show an indication of SC at $T < 1$ K, zero resistivity cannot be achieved down to 50 mK. Such a sensitivity in SC to sample purity would imply an unconventional pairing mechanism as observed in heavy-fermion superconductors [2, 11], the itinerant-electron ferromagnet UGe_2 [35], and Sr_2RuO_4 [34], where the SC is destroyed when the mean-free-path of electrons l_{mfp} is smaller than the superconducting coherence length ξ. Based on the residual resistivity and the upper critical fields, Wu *et al* estimated the SC coherence length ξ ~ 185 Å, l_{mfp} ~ 766 Å and ~153 Å for a clean (RRR $>$ 200) and a dirty (RRR ~ 50) sample, respectively. The estimated values of l_{mfp} and ξ confirm that the bulk SC can be observed only in samples with $l_{mfp} > \xi$.

2.3. Follow-up investigations about the pressure-induced SC in CrAs

Since the Cr-3d states dominate the electronic density of states at the Fermi energy in CrAs, it has become the first superconductor among the Cr-based compound. This discovery has thus aroused considerable research interest followed by a number of experimental studies, including neutron diffraction [24, 25], NMR and NQR [27], μSR [29], XRD [62], as well as a new method for crystal growth and magnetotransport studies by different groups. In the following, we summarize the main results.

2.3.1. NMR and NQR. Kotegawa *et al* performed the NQR or the so-called zero-field NMR measurements under ambient and high pressures in order to elucidate the underlying electronic correlations and SC symmetry in CrAs [27]. The nuclear spin-lattice relaxation rate $1/T_1$ in the normal state under pressure reveals the presence of substantial magnetic fluctuations in the paramagnetic state, and the absence of a Hebel–Slichter coherence peak in the superconducting state is evidence of the unconventional nature of the observed SC.

The NQR spectra for ^{75}As nucleus of CrAs at ambient pressure is shown in figure 12(a). Complicated spectra with six peaks were obtained at both 5 and 100 K, which could be well described by the double helical magnetic structure mentioned above. As shown in the inset of figure 12(a), the obtained initial field $\boldsymbol{H}_{int}$ decreases gradually as the temperature increases and vanishes abruptly at T_N, consistent with the first-order nature of the transition. Figure 12(b) shows the pressure dependence of the NQR spectra measured at 5 K. The intensity of the HM state is drastically suppressed at $P = 0.74$ GPa; meanwhile another sharp spectrum corresponding to the paramagnetic (PM) state appears at ~33 MHz. The observed spectra for both the HM and PM states at 0.74 GPa gives microscopic evidence of the phase separation. A signal from the HM state could not be observed at 0.81 GPa indicating that the homogeneous PM phase is realized above ~0.8 GPa.

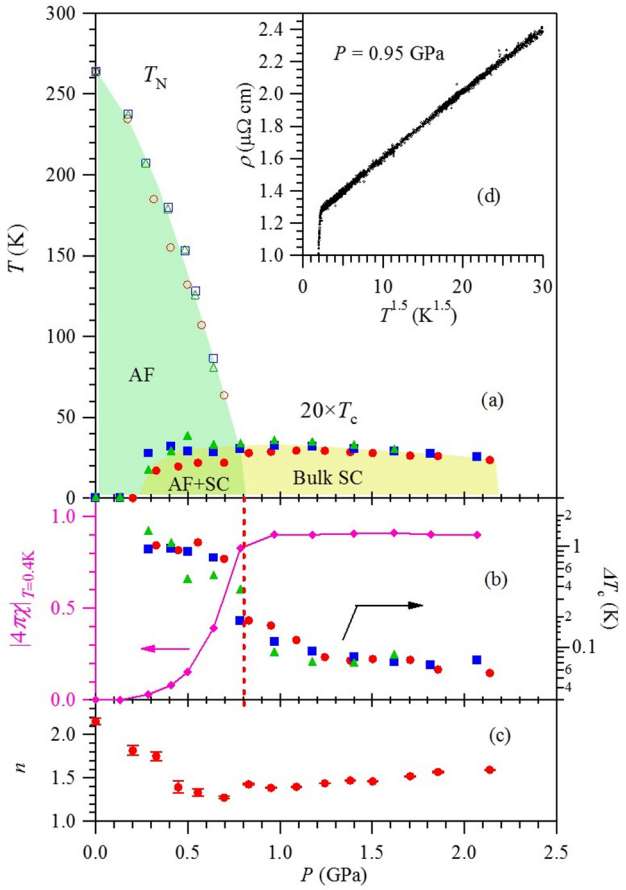

Figure 11. Temperature-pressure phase diagram of CrAs. (a) Pressure dependences of the double helical AF transition temperature T_N and the superconducting (SC) transition temperature T_c for CrAs single crystals; T_c has been scaled by a factor of 20 for clarity. (b) The superconducting shielding fraction at 0.4 K, $|4\pi\chi|_{T=0.4\,K}$, and the superconducting transition temperature width, ΔT_c, as a function of pressure. Here ΔT_c is defined as the 10%–90% superconducting transition width. (c) Pressure dependence of the low-temperature resistivity exponent, n, obtained from the power-law fitting to the normal-state resistivity below 10 K. (d) A plot of ρ versus $T^{1.5}$ for the normal-state $\rho(T)$ curve at $P = 0.95$ GPa. The circle (red), square (blue), and triangle (green) in (a)–(c) represent three independent samples with RRR = 240, 327, and 250, respectively. Reprinted by permission from Macmillan Publishers Ltd: Nature Communications [16], Copyright 2014.

The temperature dependences of $1/T_1T$ in the PM phase under various pressures are shown in figure 13. As can be seen, $1/T_1T$ is nearly temperature independent for $T > 100$ K, and increases upon cooling below ~100 K. For a Fermi liquid, T_1 obeys the Korringa law as $T_1T \sim 1/N(E_F)^2$, where $N(E_F)$ is the density of states at the Fermi level. The deviation from the Fermi liquid below ~100 K demonstrates the presence of magnetic correlations developing towards lower temperatures. The enhancement of $1/T_1T$ at low temperatures has been observed in other d-electron superconductors adjacent to magnetic phases, such as iron pnictides [63, 64], and such an enhancement is usually attributed to the spin fluctuations of d electrons.

The temperature dependence of $1/T_1T$ under 0.81 GPa below 5 K is displayed in figure 14(a). T_c is determined to be 1.85 K by the temperature dependence of the change in the resonance frequency measured by an *in situ* NMR coil, as shown in figure 14(b). Below T_c, $1/T_1T$ shows a clear reduction with no signature of a Hebel–Slichter coherence peak, which is a marker of a BCS superconductor. For comparison, the solid green line shows the calculated $1/T_1T$ for a conventional BCS model with an isotropic superconducting gap of $\Delta(0)/k_BT_c = 1.8$, while the red line shows the calculated $1/T_1T$ for a line-node model with $\Delta(0)/k_BT_c = 2.6$. The experimental results show that the coherence effect is completely absent in CrAs, strongly suggesting that SC is not of the conventional type. Figure 14(c) shows the temperature dependence of $1/T_1$ at 0.81 GPa, which follows closely to $\sim T^3$ behavior below T_c. This provides further evidence for the presence of line-nodes in the superconducting gap function. However, the lowest temperature they achieved is about 0.7 K, which is not low enough compared to T_c. Further investigations of $1/T_1$ down to much lower temperatures are highly desirable.

2.3.2. Neutron diffraction. Keller *et al* [24] and Shen *et al* [25] carried out neutron diffraction (NPD) experiments under high pressure soon after the discovery of SC in CrAs. Figure 15(a) shows the pressure dependence of NPD patterns measured at 1.2 K at pressures of 0.35, 0.5, and 0.65 GPa by Keller *et al* [24]. No crystallographic or magnetic phase transition has been observed up to 0.65 GPa. Figure 15(b) shows the pressure dependence of the first magnetic satellite (0, 0, $\pm k_c$) at $P = 0.35$, 0.5, and 0.65 GPa. Apparently, the magnetic intensities decrease with pressure, which indicates a reduction of the average ordered magnetic moment. The average moment was estimated to decrease from 1.7 μ_B at ambient pressure to ~0.38 μ_B at 0.65 GPa.

Shen *et al* [25] measured the NPD at pressures up to ~1.0 GPa. They found a spin reorientation from the *ab* plane to the *ac* plane, along with an abrupt drop of the magnetic propagation vector at a critical pressure $P_c \approx 0.6$ GPa. As shown in figure 16, the diffraction pattern at $P = 0.6$ GPa shows substantial changes in the magnetic reflections compared to those at ambient and low pressures, indicative of a magnetic phase transition. The refinement analyses revealed that these changes originate from a spin reorientation from the *ab* to the *ac* plane, as illustrated in figures 16(a) and (b). Figure 17(a) displays the pressure and temperature dependence of the propagation vector, which decreases gradually with decreasing temperature between 0 and 0.4 GPa when the magnetic moment remains in the *ab* plane. At $P_c \approx 0.6$ GPa, the propagation vector exhibits a quick decrease on cooling through the spin-reorientation temperature $T_r = 88$ K.

Figure 17(b) plots the structural and magnetic phase diagram of CrAs under pressure based on the NPD study. The neutron data show that the magnetic order and structural distortion persist at $P = 0.72$, 0.82, and 0.88 GPa, and eventually completely disappear at $P \approx 0.94$ GPa. More interestingly, the contour propagation vector map and the superconducting transition temperature plot reveal that the emergence of SC is associated with the spin reorientation and the decrease in the propagation vector. Moreover, the Cr magnetic moments tend to be aligned antiparallel between the nearest neighbors with increasing pressure toward the optimal SC regime. These results indicate a strong interplay between magnetism and SC in this system [25].

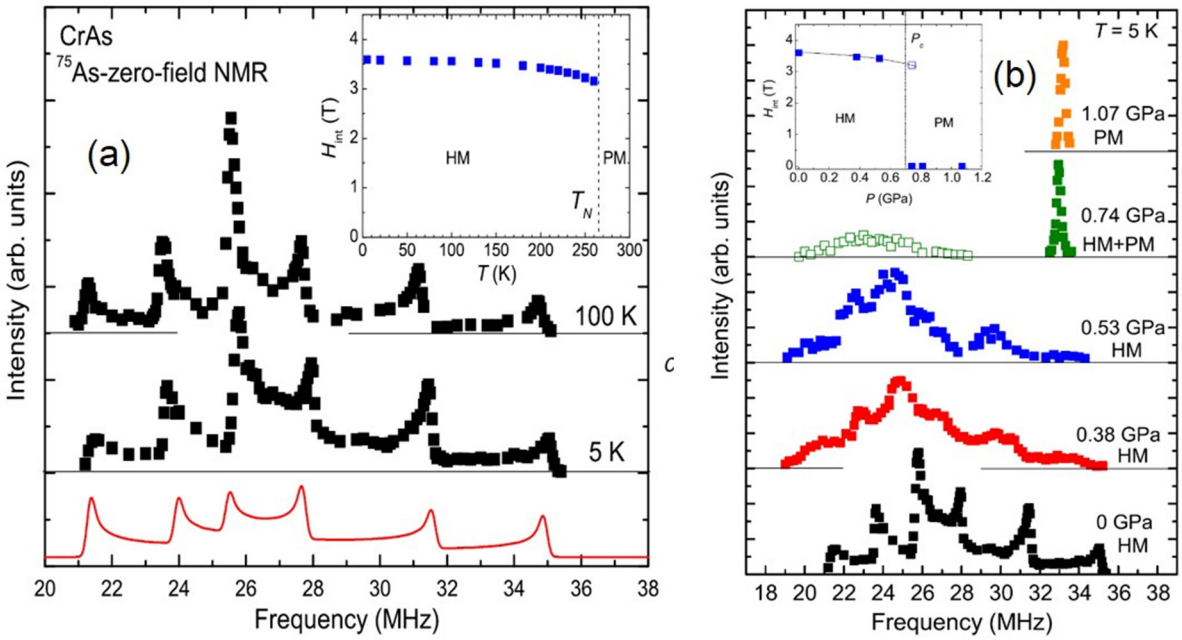

Figure 12. (a) The ^{75}As NQR spectra at ambient pressure. The spectrum can be reproduced based on the double helical magnetic structure as show in the bottom solid line. The inset shows the temperature dependence of initial field H_{int}. (b) Pressure dependence of ^{75}As NQR spectra at 5 K. Phase separation between the HM and PM phases occurs in the vicinity of P_c. Reprinted figure with permission from [27], Copyright 2015 by the American Physical Society.

It should be noted that there is some discrepancy in the above neutron studies [24, 25]. The former showed that the magnetic structure does not change up to 0.65 GPa, while the latter study found a magnetic phase transition associated with the spin reorientation and a dramatic decrease of the propagation vector on cooling through T_r at $P = 0.6$ GPa. The disparity might arise from the different pressure medium used. A fluorocarbon-based fluid pressure medium was used by Keller *et al* [24] which could cause pressure inhomogeneity, while helium was employed as the pressure medium by Shen *et al* [25] to minimize pressure inhomogeneity.

2.3.3. Muon spin rotation (μSR). Similar to NMR, μSR is a powerful local probe to detect the magnetic properties and superconducting mechanism. Khasanov *et al* studied the magnetic response of polycrystalline CrAs with zero-field and weak transverse field μSR experiments under pressures up to 1 GPa [29]. They found that the magnetism remains bulk up to $P \simeq 0.35$ GPa while its volume fraction gradually decreases with increasing pressure until it vanishes at $P \simeq 0.7$ GPa. The superconducting and magnetic volume fractions are spatially phase separated.

Figure 18 summarizes the zero field and weak transverse field μSR data. At ambient pressure, the long-range helical order below T_N is confirmed by the spontaneous muon spin precession (figure 18(a)), and the oscillating part of the signal can be accurately described by a field distribution characterized by a minimum (B_{min}) and a maximum (B_{max}) cutoff field (inset of figure 18(a)), which is consistent with an incommensurate HM order. The magnetism occupies close to 100% of the sample volume at low pressures below 0.35 GPa, and the sample is separated into a magnetically ordered phase and a non-magnetic

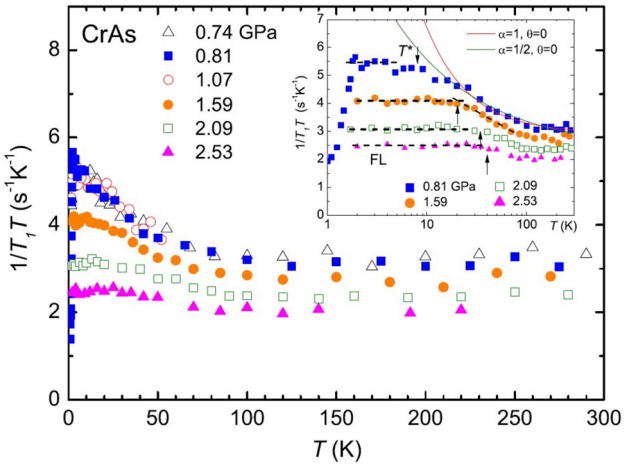

Figure 13. Temperature dependence of $1/T_1T$ in the paramagnetic state under various pressures. The increase in $1/T_1T$ towards low temperatures demonstrates the development of the magnetic fluctuations. The inset shows the same data between 0.81 and 2.53 GPa in a logarithmic scale. Reprinted figure with permission from [27], Copyright 2015 by the American Physical Society.

phase above 0.35 GPa (figures 18(a) and (b)). For $P > 0.7$ GPa, the μSR experiments proved the absence of magnetic order as exemplified by the weakly damped μSR time spectra.

Khasanov *et al* [29] also studied the superfluid density $\rho_s(0)$ in the phase coexistence region. The superfluid density was found to scale with T_c as $\rho_s \propto T^2$ (figure 19) and suggests a conventional BCS mechanism of the Cooper-pairing in CrAs. It should be noted that the SC in CrAs is very sensitive to sample purity, and only high-quality single crystals with RRR > 200 show bulk SC, whereas the samples used by Khasanov *et al* [29] are polycrystalline with reduced T_c.

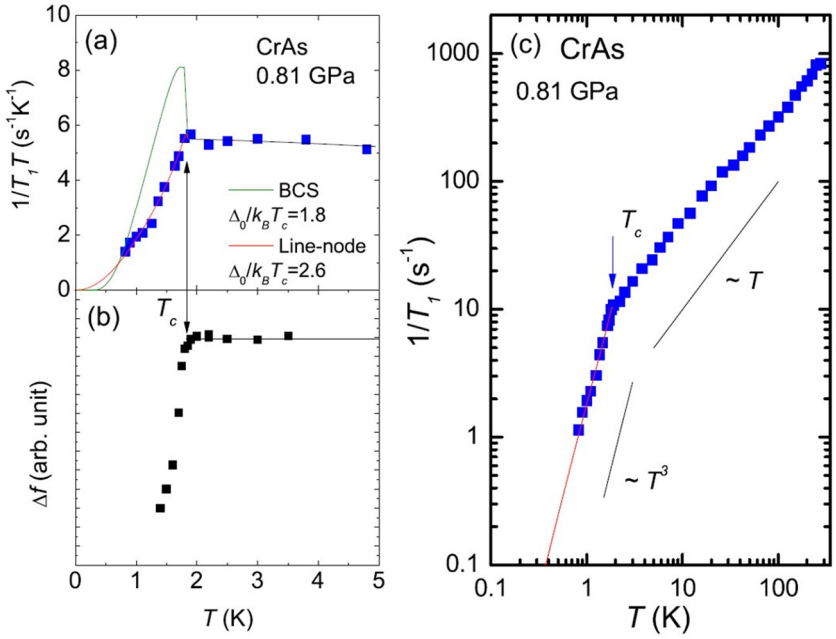

Figure 14. (a) Temperature dependence of $1/T_1T$ below 5 K at 0.81 GPa. The absence of a coherence peak at T_c indicates unconventional SC. (b) The change in the resonance frequency of the NMR coil near T_c. (c) Temperature dependence of $1/T_1$. The T^3 dependence below T_c signifies line nodes in the gap function. Reprinted figure with permission from [27], Copyright 2015 by the American Physical Society.

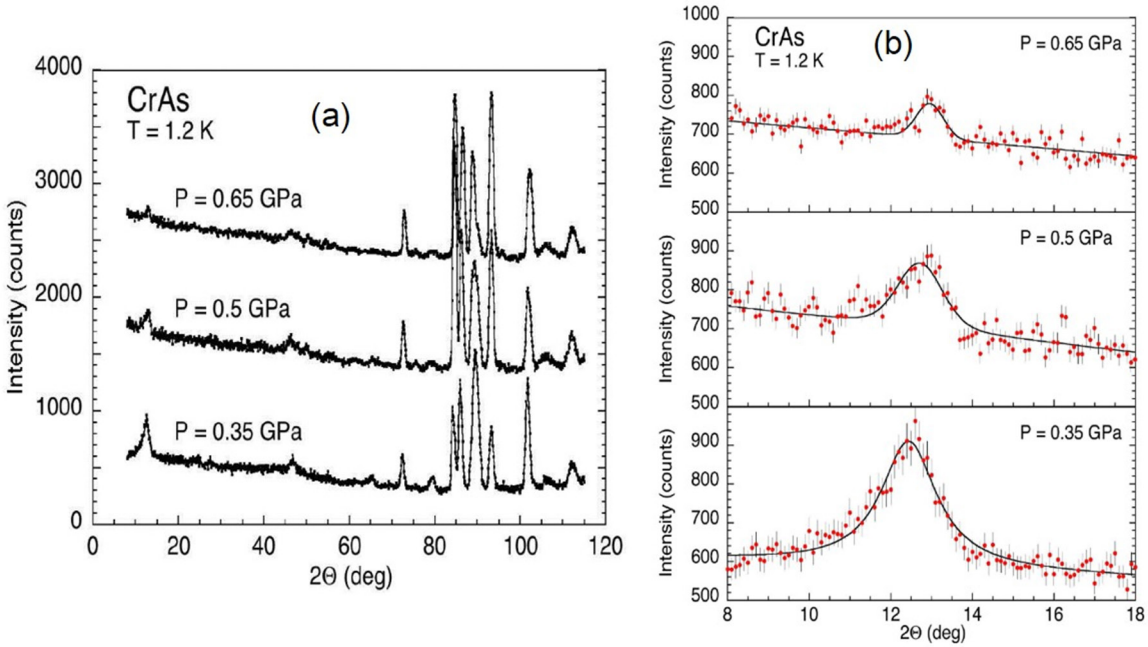

Figure 15. (a) The NPD patterns for CrAs at 1.2 K under different pressures $P = 0.35$, 0.5 and 0.65 GPa. (b) Pressure dependence of the first magnetic satellite (0, 0, $\pm k_c$). Reprinted figure with permission from [24], Copyright 2015 by the American Physical Society.

Thus, high-pressure μSR experiments on high-quality single crystals are highly desirable.

2.3.4. Synchrotron XRD. Since the magnetic order correlates tightly with the structural transition in CrAs, Yu *et al* investigated the structural evolution under pressure by using angle-dispersive XRD [62]. The lattice parameters and volume of CrAs as a function of pressure are given in figures 20(a)–(d). The interesting result is that parameters a and c exhibit a non-monotonic change, and the lattice parameter b undergoes a rapid contraction at ~0.18–0.35 GPa, which suggests a pressure-induced isostructural phase transition. The obtained transition pressure coincides with that of the emergence of pressure-induced SC in CrAs [16]. Above 0.35 GPa, the axial compressibilities of CrAs present remarkable anisotropy.

2.3.5. Other developments in CrAs. Progress has been made regarding the new method for CrAs crystal growth. Wu *et al* grew the CrAs single crystals with the Sn flux method [47]. Recently, Zhu *et al* reported the growth of CrAs single crystals

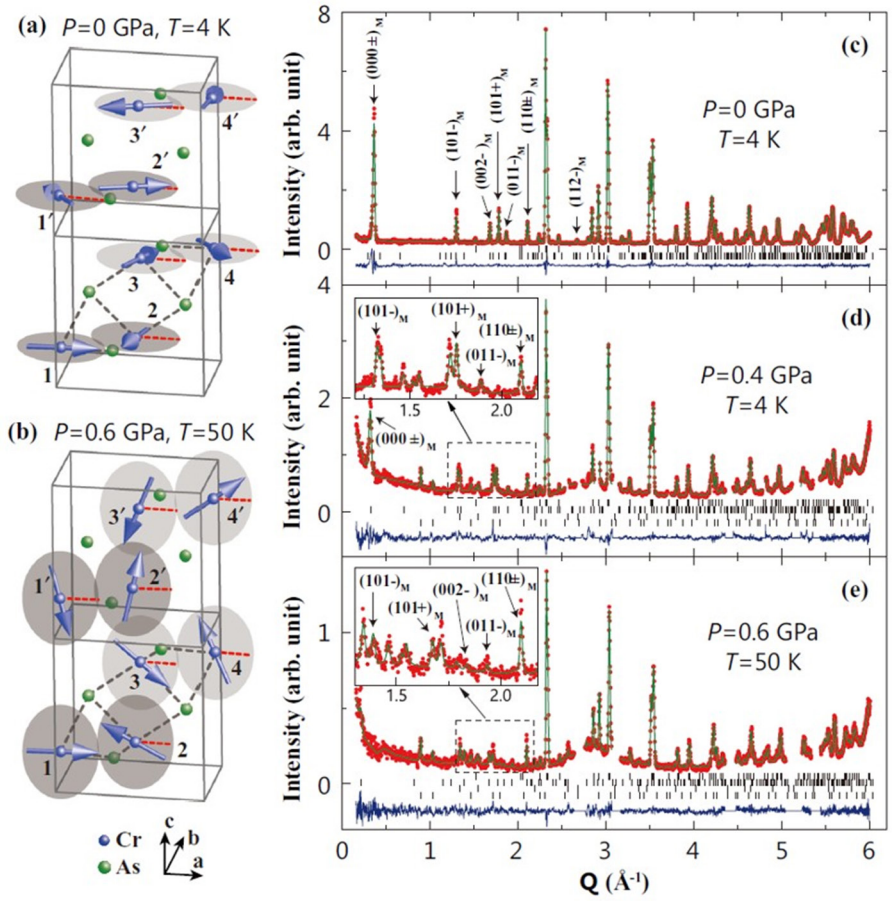

Figure 16. The NPD patterns and magnetic structures at different pressures for CrAs. (a) and (b) Magnetic structures at ambient pressure and 0.6 GPa, respectively. (c)–(e) The diffraction intensities at ambient pressure and 4 K (c), 0.4 GPa and 4 K (d), and 0.6 GPa and 50 K (e), respectively. Reprinted figure with permission from [25], Copyright 2016 by the American Physical Society.

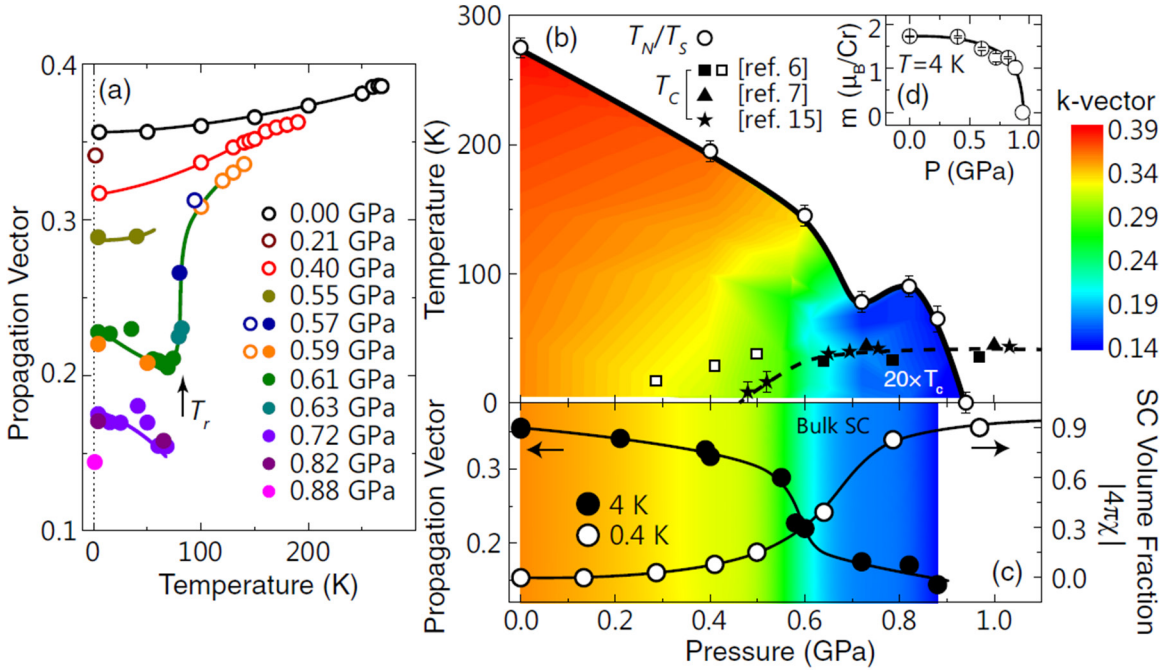

Figure 17. (a) Temperature and pressure dependence of the magnetic propagation vector. The open and solid circles indicate the magnetic moment in the *ab* and *ac* plane, respectively. (b) Structural and magnetic phase diagram of CrAs. The inset shows the pressure dependence of Cr moments. (c) The pressure dependence of the propagation vector and the superconducting volume fraction. Reprinted figure with permission from [25], Copyright 2016 by the American Physical Society.

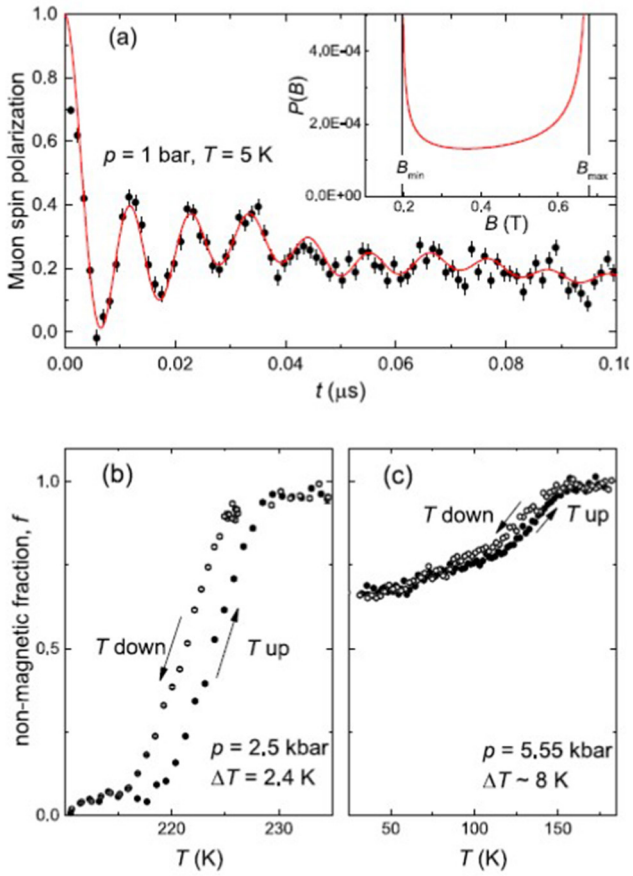

Figure 18. (a) Zero-field μSR time-spectra of CrAs at 5 K and ambient pressure. The solid line is a fit according to the theoretical field distribution caused by the incommensurate helimagnetic order shown in the inset. (b) and (c) The temperature dependence of non-magnetic volume fraction f of CrAs obtained in the wTF μSR at 2.5 kbar and 5.55 kbar, respectively. A clear hysteresis is indicative of a first-order magnetic transition. Reproduced from [29]. CC BY 4.0.

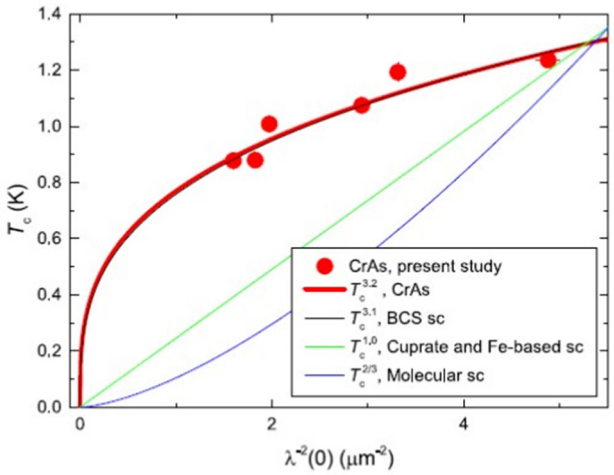

Figure 19. Superconducting transition temperature T_c versus inverse square zero-temperature magnetic penetration depth $\lambda^{-2}(0)$ for CrAs. The red line is $\lambda^{-2}(0) \propto (T_c)^n$ fit with the exponent $n = 3.2$ (2). The black, green, and blue lines are empirical relations for some phonon-mediated BCS superconductors ($n = 3.1$), cuprate and Fe-based high-T_c superconductors ($n = 1$), and molecular superconductors ($n = 2/3$), respectively. Reproduced from [29]. CC BY 4.0.

with dimensions of ~1 × 5 × 1 mm^3 via the chemical vapor transport method [65]. Resistivity and magnetization measurements were performed which showed similar behavior as reported by Wu *et al*, except that the resistivity shows a sharp jump rather than a drop right below T_N upon cooling.

A further development has been made regarding the magnetotransport measurements by Niu *et al* [66], who studied the magnetoresistance (MR = $[\rho(H) - \rho(0)]/\rho(0) \times 100\%$) of CrAs crystals down to 16 mK under pressure up to 1.8 GPa. They observed a large and quasilinear MR from the upper critical field to 14 T at low temperatures. The MR reached over 120% at 16 mK and 14 T. The linear behavior of MR in correlated material is rare. They interpreted the large quasilinear MR in terms of an interplay between a nontrivial band crossing protected by nonsymmorphic crystal symmetry and strong magnetic fluctuations.

3. MnP

3.1. Physical properties of MnP at ambient pressure

3.1.1. Magnetic structures of MnP. Similar to CrAs, MnP crystallizes in an orthorhombic B31 structure. The convention of $a > b > c$ has been commonly used in the literature to define the orthorhombic cell in the *Pbnm* space group. For consistency with CrAs in the present paper, we employ the standard notation of $c > a > b$ for the *Pnma* space group with the unit-cell dimensions of $a = 5.258$ Å, $b = 3.172$ Å, and $c = 5.918$ Å, respectively.

The earliest studies on the magnetic properties of MnP can be traced back to 1929 [67, 68]. Before realizing the importance of itinerant-electron ferromagnetism, the initial interest in MnP arises from the fact that the extrapolated spontaneous saturation moment $M_s \sim 1.2\ \mu_B$/Mn is substantially lower than the observed effective paramagnetic moment $\mu_{eff} \sim 3\ \mu_B$, leading to speculations of either two-sublattice ferrimagnetism or a canted-spin model. The magnetic properties of a MnP single crystal were first studied in 1963 by Huber and Ridgley [20, 21], who grew the single crystal in a two-zone furnace. Their results confirmed the occurrence of a PM–FM transition at $T_C = 291.5$ K. The Curie–Weiss fitting to the PM susceptibility yields a Curie temperature $\theta_{CW} = 312$ K and $\mu_{eff} = 2.9\ \mu_B$/Mn; the extrapolated saturation moment was found to be $M_s = 1.3\ \mu_B$. In the FM region, MnP exhibits a strong magnetic anisotropy, i.e. the easy direction of magnetization is the b axis and the hard direction is the c axis. In addition, they observed another transition at $T_s = 50$ K, below which MnP is metamagnetic, i.e. it exhibits an AF–FM transition which is a function of applied field and temperature.

Goodenough had rationalized the observed reduced saturation moment on the basis of the narrow 3d-band model and further predicted a simple cycloidal spiral magnetic structure below T_s [69]. The magnetic structures of MnP were experimentally determined with NPD experiments by Forsyth *et al* [22] at 4.2 K and by Felcher [23] in the temperature range between 4.2 and 78 K. These experiments confirmed directly that MnP is FM for $T_s < T < T_C$ with the Mn moment ~1.3 μ_B directed along the orthorhombic b axis, and then takes below T_s a double helical structure in which the

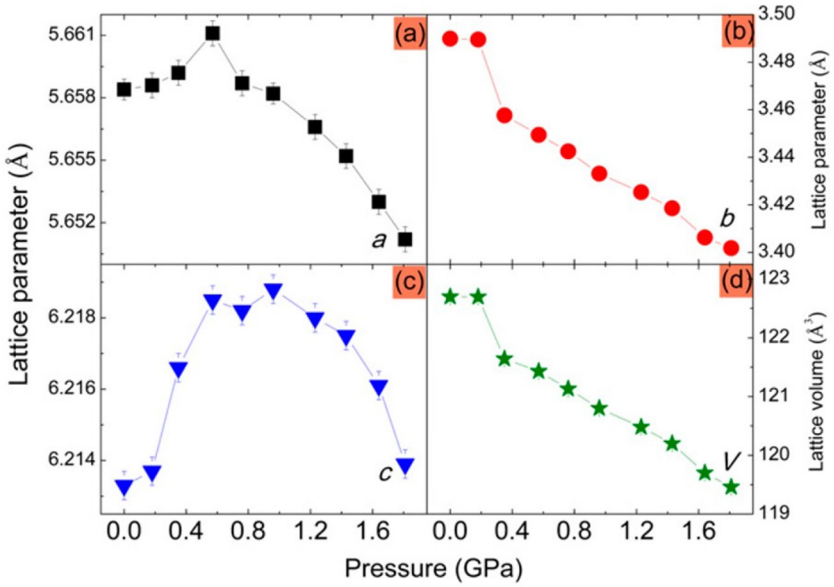

Figure 20. Pressure dependences of the lattice parameters (a) a, (b) b, (c) c, and (d) volume of CrAs. Reproduced with permission from [62].

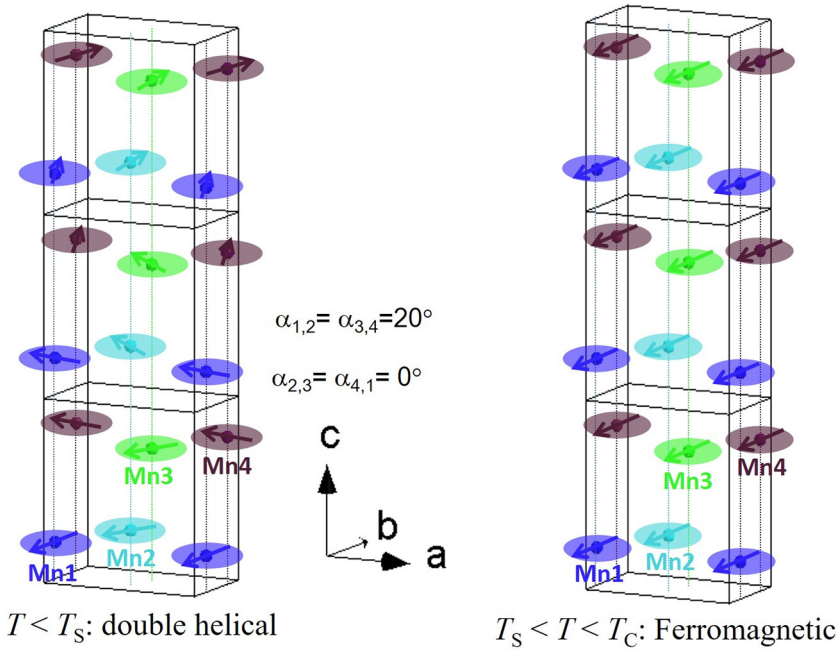

Figure 21. The magnetic structures of MnP at ambient pressure: the double helical order at $T < T_s$, and the ferromganeic state at $T_s < T < T_C$. Reproduced from [22]. © IOP Publishing Ltd. All rights reserved.

Mn spins rotate within the ab plane with the propagation vector $\mathbf{q} = 0.112 \times 2\pi c^*$ along the c axis. Figure 21 illustrates these magnetic structures of MnP. It should be noted that although CrAs and MnP share similar double helical magnetic structures at low temperatures, their different propagation vectors, i.e. $0.354 \times 2\pi c^*$ versus $0.112 \times 2\pi c^*$, give rise to dominant AF and FM interactions, respectively. Later on, Moon performed neutron polarization experiments to study the details of the spiral structure of MnP [70]; the departure from the unity of the ratio of spin-flip scattering to non-spin-flip scattering of the $(0, 0, 2 \pm\delta)$ satellites indicates an elliptical spiral or a distorted circular spiral with bunching along the easy axis.

3.1.2. Magnetic phase diagrams of MnP under external fields. The appearance of a double helical (or screw) order and metamagnetism below T_s suggests the presence of temperature-dependent, competing AF and FM interactions. The strong magnetocrystalline anisotropy and metamagnetism were the subject of extensive investigations during the 1960s and 1970s in that a variety of magnetic phases including the FM, screw (SCR), fan, or cone-type ordering can appear depending on the temperature, the magnitude and the direction of external magnetic fields [71–75]. Because of the richness of its magnetically ordered phases, MnP was subsequently studied in the 1980s as a model system for phase-transition physics, especially in the context of the Lifshitz

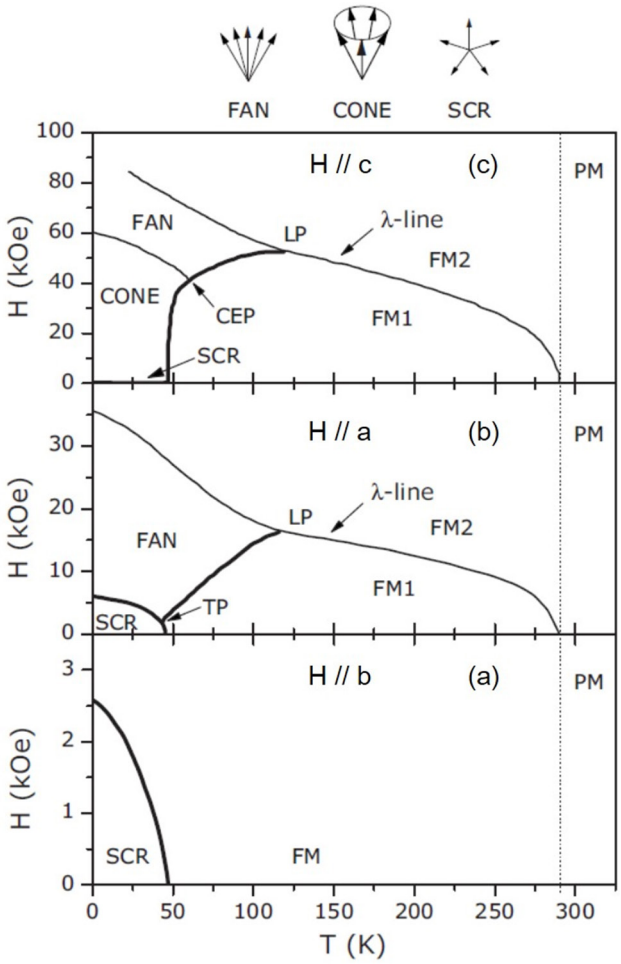

Figure 22. Magnetic phase diagrams of MnP single crystal for the external field applied along the three pricinpal axes of the orthorhombic cell (*Pnma*): (a) *H*//*b*, (b) *H*//*a*, and (c) *H*//*c*. The labels have the following meaning: PM-paramagnetic phase, FM-ferromagnetic phase, SCR-screw phase, FM1-magnetic moment along the easy (*b*) axis, FM2-magnetic moment along the applied magnetic field, CEP-critical end point, TP-triple point, and LP-Lifshitz point. The thick and thin lines represent first and second order transitions, respectively. The spin arrangements for the screw, fan, and cone phases are illustrated at the top of the figure. Reprinted figure with permission from [82], Copyright 2008 by the American Physical Society.

multicritical point in a magnetic system [76–80]. Figure 22 depicts the magnetic phase diagrams of MnP for the external magnetic field applied along the three principal axes of the orthorhombic lattice [81, 82].

(i) Figure 22(a) shows the phase diagram for *H*//*b* (the easy axis), which is the simplest case. Upon increasing the magnetic field at $T < T_s$, the SCR phase changes back to the FM phase with a first-order character; the SCR–FM phase boundary is denoted by a thick line in figure 22(a).

(ii) Figure 22(b) shows the phase diagram for *H*//*a* (the intermediate axis), which contains two triple points. Similarly, when the temperature is decreased under low fields, MnP first becomes FM (denoted as FM1 for the moments directed along the *b* axis) at T_C, and then undergoes a first-order transition at T_s from FM1 to the SCR structure. Upon increasing the magnetic field at $T < T_s$, the screw phase changes to the fan (FAN) structure, in which the magnetic moment does not perform a full rotation in the *ab* plane but oscillates about the *a* axis like a fan. A further increase in the magnetic field leads to a fully polarized arrangement, which is denoted as FM2 in that the moments are aligned along the *a* axis. When the magnetic field is applied at temperatures slightly above T_s, the system will undergo successive transitions from FM1 to FAN, and then to the FM2 phase, with the FM1–FAN phase boundary connecting the SCR and the FM2 phase. The lower triple point where SCR, FAN, and FM1 meet is located at $T = 45.4$ K and $H = 2.48$ kOe, while the upper one where the FAN, FM1 and FM2 meet is determined as $T = 121 \pm 1$ K and $H = 16.5$ kOe. For temperatures above 121 K, the FM1 transforms to the FM2 phase via a second-order transition. The upper critical point is also called the Lifshitz point (LP) [76, 77], where the FAN–FM2 and the FM1–FM2 phase boundaries merge into the λ line. The phase boundaries near the LP were carefully determined to be tangent to each other, and detailed studies on the LP of MnP can be found in [76–80]. All the transitions between the magnetically ordered phases (i.e. FM1–SCR, FM1–FAN, SCR–FAN) are of first order, while the transitions to the FM2 phase are of second order.

(iii) Figure 22(c) shows the phase diagram for *H*//*c* (the hard axis), in which the SCR phase exists only at zero field. For $T < T_s$, the application of the external magnetic field first changes the SCR phase to a CONE phase, which is similar to the SCR phase but exhibits a component along the *c* axis, and then a change to the FAN phase with the moments oscillating about the *c* axis, and eventually fully polarizes the system into the FM2 phase with the moments directed along the *c* axis. For $T > T_s$, the FM1 phase will intersect the CONE–FAN boundary at a critical end point (CEP) and meet the FAN and FM2 phase at the LP. From T_s to the CEP, the system changes from FM1 to the CONE, FAN, and then to the FM2 states with increasing magnetic fields. Between CEP and LP, the system changes from FM1 to FAN and then to FM2 upon an increase in the magnetic fields. For temperatures above LP, FM1 changes to FM2 via a second-order transition. Other transitions involving FM1 are of first order.

3.1.3. Transport properties of MnP. The temperature dependence of resistivity $\rho(T)$ for MnP shows metallic behavior with characteristic anomalies at the magnetic transitions. A cusp-like anomaly typical for a metallic ferromagnet appears at T_C, while the *c*-axis resistivity exhibits an obvious dip at T_s because the spiral propagates along the *c* axis [83, 84]. These resistivity anomalies can be used to track down their evolutions under pressure. By investigating the $\rho(T)$ of MnP crystals grown with different methods, Takase and Kasuya [84] demonstrated that unlike T_C, T_s can vary from 46 K to 53 K depending sensitively on the sample purity. The crystal with a smaller RRR shows a lower T_s. In addition, the Fermi-liquid behavior of $\rho \propto T^2$ was observed for all the different magnetically ordered phases listed above. A large resistivity

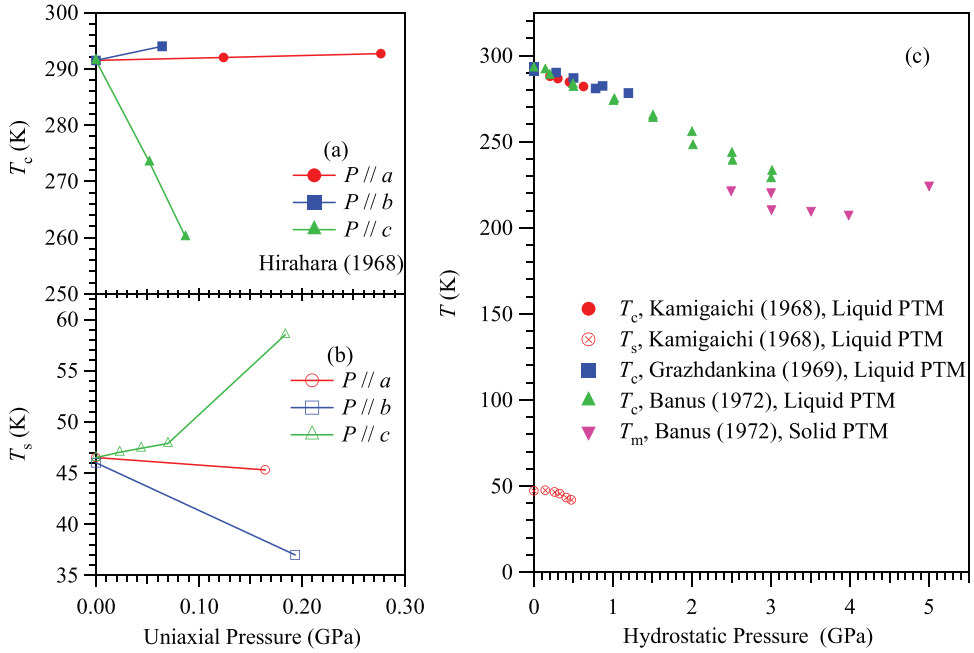

Figure 23. The magnetic transition temperatures T_C and T_s of MnP as a function of (a) and (b) the uniaxial pressure, and (c) the hydrostatic pressure.

coefficient suggests that the electron–electron scattering is dominant at low temperatures and the Fermi surfaces are composed of mainly Mn-3d electrons, which is consistent with low-temperature specific heat analysis [85] and the theoretical electronic–structure calculations [86, 87].

Yanase and Hasegawa [86] reported a self-consistent APW calculation of the spin-polarized energy band structure for MnP. The density of states near the Fermi energy is dominated by the Mn-3d electrons. For the minority spin electron, bands near the Fermi energy, E_F, consist mainly of Mn 3d states and have a high density of states. Bands for a majority spin electron have a low density of states at E_F. MnP should be considered as a covalent material and the calculated total spin moment is ~1.2 μ_B/Mn, which is close to the experimental value of 1.3 μ_B/Mn. The calculated exchange splitting is about 1.6 eV, about the same as that for Fe, and thus MnP can be considered as a strong itinerant-electron ferromagnet.

3.1.4. Effect of pressure on the magnetic transitions of MnP. As mentioned above, the observations of double-helical order and the metamagnetism in MnP suggest the presence of competing AF and FM interactions. The effect of pressure on the magnetic transition temperatures of MnP was studied nearly 40 years ago to probe the variation of these interactions with volume [88–91]. Hirahara *et al* first investigated the effect of uniaxial pressure on magnetic interactions in the MnP single crystal [88]. As shown in figures 23(a) and (b), for *P*//*c*, T_C decreases quickly with a huge negative pressure coefficient of $-360\,\mathrm{K\,GPa^{-1}}$, while T_s increases with pressure and seems to grow faster above 0.1 GPa. The pressure dependences of T_C and T_s are reversed when the pressure is applied within the *ab* plane, i.e. $dT_C/dP > 0$ and $dT_s/dP < 0$, and the pressure coefficients for *P*//*a* are much smaller than those for *P*//*b* (see also table 2). These results suggest that the compression along the *c* axis (the *ab* plane) will weaken (strengthen) the FM interactions, but strengthen (weaken) the AF interactions in MnP, at least in the investigated pressure range.

The application of hydrostatic pressure is expected to be a combination of these anisotropic uniaxial pressure effects. Figure 23(c) summarizes the pressure dependences of T_C and T_s under hydro- or quasi-hydrostatic pressure conditions reported previously. As can be seen, T_C decreases gradually with pressure up to 3 GPa with a negative pressure coefficient $dT_C/dP \sim -20\,\mathrm{K\,GPa^{-1}}$ under a relatively good hydrostatic pressure condition by employing the liquid pressure transmitting medium (PTM). Banus [91] noticed that the shape of the ac magnetic susceptibility curve changes at 3 GPa to a cusp-like anomaly, which is characteristic of an AF order. When the AgCl solid PTM was used for $P > 3$ GPa, it was observed that T_C keeps nearly constant up to 4 GPa, and then increases slightly under higher pressures. Based on the arguments by Goodenough, Banus had attributed the pressure-induced FM–AF transition to band broadening that approaches the limiting bandwidth supporting spontaneous magnetism [91]. The pressure dependence of T_s had been investigated up to ~0.5 GPa by Kamigaichi *et al* [89]. As shown in figure 23(c), T_s initially remains nearly unchanged to 0.2 GPa, in accordance with the sum of the uniaxial pressure effects on T_s shown in figure 23(b), and then T_s decreases gradually with a further increase in pressure.

3.2. Pressure-induced SC in MnP [17]

Soon after the discovery of pressure-induced SC in CrAs [16], we immediately turned our attention to the isostructural helimagnetic MnP, with the aim of realizing its magnetic QCP under pressure and to explore the possible SC. Based on the previous high-pressure studies shown in figure 23(c),

Table 2. Pressure coefficients of T_C and T_s reported in the literature.

Pressure conditions		Measured pressure range (GPa)	dT_c/dP (K Gpa^{-1})	dT_s/dP (K GPa^{-1})	Ref.
Uniaxial pressure	*P//a*	0–0.3	4.4	−7.3	[88]
	P//b	0–0.2	38.9	−46.5	[88]
	P//c	0–0.2	−360	68.3	[88]
Hydrostatic pressure	Liquid PTM	0–0.6	−15	−20	[89]
	Liquid PTM	0–1.2	−11.4	/	[90]
	Liquid PTM	0–2	−18.5	/	[91]
	Liquid PTM	2–3	−25	/	[91]

however, such an expectation seems to be elusive given an unusual enhancement of T_C above 4 GPa. Nevertheless, we noticed that the AgCl solid PTM was employed in the previous study for $P > 3$GPa, where the nonhydrostatic pressure conditions can alter the intrinsic pressure effect. In addition, the pressure and temperature ranges in the previous studies were far from the magnetic QCP. We therefore just gave a shot of MnP single crystal by performing high-pressure resistivity measurements with the cubic anvil cell apparatus that can maintain relatively good hydrostatic pressure conditions above 10 GPa. In this case, we used glycerol as the liquid PTM. We found, surprisingly, that MnP becomes superconducting below $T_c \approx 1$ K near the magnetic QCP at $P_c \approx 8$ GPa. Details have been published in [17]. We present the essential high-pressure results below.

3.2.1. Suppression of magnetic transitions under pressure. The MnP single crystals used in our study were also grown out of the Sn flux and have a needle shape with the longest dimension along the *b* axis. These flux-grown MnP crystals usually show a high purity with RRR ranging from ~500–1200. As shown in figure 24(a), the *b*-axis $\rho(T)$ under various pressures up to 10.7 GPa illustrate the evolution of T_C under pressure. At ambient pressure, the FM transition at $T_C = 291$ K is manifested as a kink anomaly in $\rho(T)$, which can be defined clearly as a sharp peak in the $d\rho/dT$ curve (figure 24(b)). The $\rho(T)$ and $d\rho/dT$ curves at 2.8 GPa maintain essentially similar features as those at ambient pressure, except that T_C has been shifted down to ~250 K. Upon a further increase in pressure to 5.0 GPa, however, $\rho(T)$ exhibits distinct features showing a clear inflection point at ~200 K, which corresponds to a step-like anomaly in the $d\rho/dT$ curve in figure 24(b). We have attributed such a change in the resistivity anomaly to the fact that the FM transition changes to an AF type for $P > 3$ GPa [91]. We thus label the transition temperature as T_m for $P > 3$ GPa. The $\rho(T)$ and $d\rho/dT$ curves at 6.4 GPa are similar to that at 5.0 GPa, except that the magnetic transition broadens up and moves down to ~120 K. For $P = 7.4$ GPa, nevertheless, $\rho(T)$ changes again with the concave curvature restored for $T > T_m = 70$ K, which is manifested as a relatively broad peak in the $d\rho/dT$ curve in figure 24(b). Above this pressure, no clear anomaly can be discerned in the $\rho(T)$ curves. The complete suppression of the magnetic transition in the present work is in sharp contrast with the earlier high-pressure study by Banus [91], who found that the magnetic transition temperature is almost pressure independent or even slightly increased with pressure for $3 < P < 5$ GPa when using the solid PTM (AgCl). This comparison suggests that the magnetic transitions of MnP are very sensitive to the nonhydrostatic pressure conditions, presumably due to the strong anisotropic uniaxial pressure effects shown in figures 23(a) and (b).

The pressure dependence of T_s was monitored by measuring the *c*-axis resistivity $\rho_c(T)$ in a piston-cylinder cell. As seen in figure 24(c), $\rho_c(T)$ at ambient pressure exhibits a clear dip anomaly at T_s, which decreases monotonically with pressure and vanishes completely at ~1 GPa. We also directly followed the evolution with pressure of the magnetic transitions at T_C and T_s with the ac magnetic susceptibility $\chi'(T)$ under pressure. As shown in figure 24(d), they manifest as a sudden jump and drop, respectively, and the FM state corresponds to the in-between plateau. In agreement with the $\rho(T)$ data, T_C decreases continuously, and T_s vanishes completely around 1.4 GPa. Surprisingly, a new two-step transition denoted as T^* emerges above 1.4 GPa and increases quickly with pressure. Since no anomaly in $\chi'(T)$ can be discerned at 4.2 GPa, the magnetic transitions reflected in $\rho(T)$ above 3 GPa should correspond to an AF one.

3.2.2. Discovery of SC near the magnetic QCP. The application of pressure quickly eliminates the HM state, and first reduces the FM transition at T_C, and then changes it to an AF type for $P > 3$ GPa. The magnetic transition monitored by the anomaly in $\rho(T)$ eventually vanishes completely around $P_c \approx 8$ GPa, where the most striking change takes place at low temperatures. As shown in figure 25(a), a resistivity drop starts to emerge below 1 K at 7.6 GPa, and a more pronounced drop with an onset temperature of ~1 K can be clearly observed near the critical pressure $P_c \approx 7.8$ GPa, signaling the possible occurrence of SC. Unfortunately, such an anomaly shifts to lower temperatures with a further increase in pressure. Although zero resistivity can be hardly achieved even when the applied electrical current is reduced to 10 μA, the ac magnetic susceptibility, $4\pi\chi(T)$, shown in figure 25(b), provides strong evidence for the occurrence of SC near P_c. In perfect agreement with the $\rho(T)$ data, the diamagnetic signal appears below $T_c \approx 1$ K at 7.6 GPa, and the superconducting shielding fraction reaches ~95% of the sample volume at 7.8 GPa. A further increment of pressure to 8.6 GPa lowers T_c to below 0.5 K, while the superconducting shielding fraction remains nearly constant. Such a perfect diamagnetic response rules out the possibility of filamentary SC or impurity phases. However, the absence of zero resistivity could be caused by

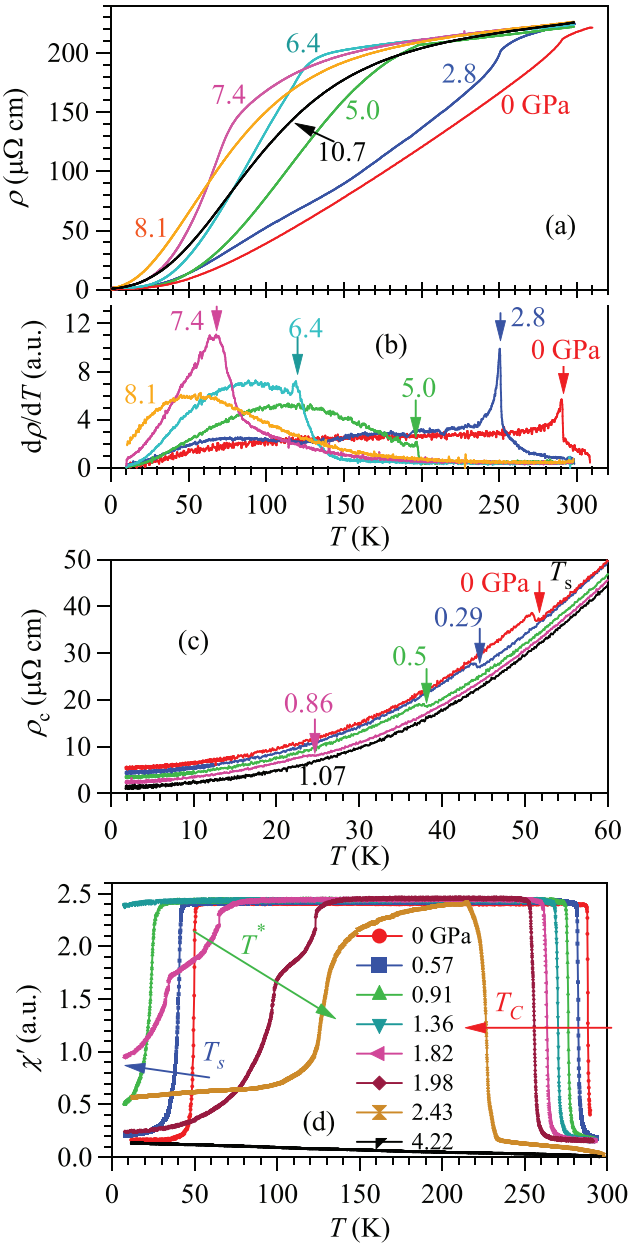

Figure 24. (a) Resistivity $\rho(T)$ and (b) the temperature derivative $d\rho/dT$ of the MnP single crystal under various pressures up to 10.7 GPa highlighting the variation with pressure of the magnetic transition indicated by the vertical arrows. (c) The c-axis $\rho_c(T)$ data at low temperatures highlighting the evolution with pressure of the double helical transition at T_s. (d) Temperature dependence of the ac magnetic susceptibility $\chi'(T)$ measured under various pressures, which signifies the appearance of a new magnetic transition at T^*. Reprinted figure with permission from [17], Copyright 2015 by the American Physical Society.

the pressure inhomogeneity or the presence of defects and cracks that have a stronger influence on the transport than the magnetic properties. The observation that the SC disappears quickly after the magnetic transition vanishes completely highlights that the pressure-induced SC has an intimate correlation with the magnetic critical point.

3.2.3. T–P phase diagram of MnP. Figure 26(a) shows the T–P phase diagram of MnP depicting explicitly the variations of

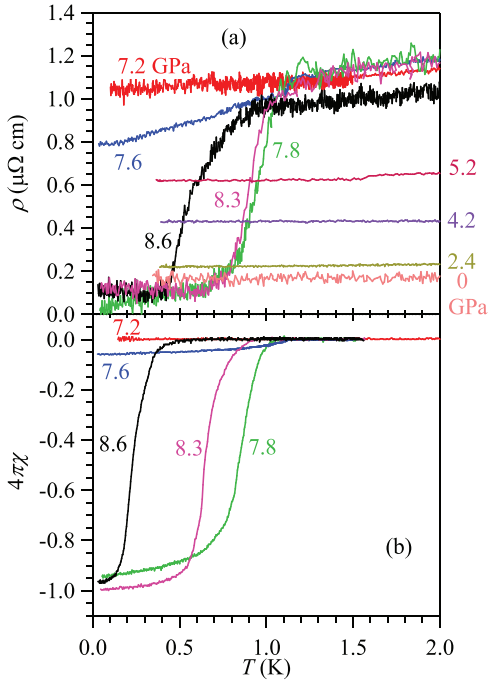

Figure 25. Temperature dependence of (a) the resistivity $\rho(T)$ and (b) the ac magnetic susceptibility $4\pi\chi$ on MnP at low temperatures under various pressures near the critical pressure. Reprinted figure with permission from [17], Copyright 2015 by the American Physical Society.

the transition temperatures, T_C, T_m, T_s, T^*, and T_c, with pressure. As can be clearly seen, the application of high pressure continuously reduces the magnetic transition temperatures, T_C and then T_m, and finally suppresses the magnetic order around $P_c \approx 8$ GPa. SC with a maximum $T_c \approx 1$ K emerges and exists within a narrow pressure range near the critical pressure P_c. The obtained superconducting T–P phase diagram for MnP is remarkably similar to that of heavy-fermion superconductors, such as $CeIn_3$ and $CePd_2Si_2$ [11], in which a magnetically mediated mechanism is believed to play a dominant role for forming Cooper pairs. The situation in MnP is more complicated since the FM transition changes to an AF type around 3 GPa. Although the nature of the new AF state has been left for future studies, as detailed below, we first provided some evidence that is in favor of an AF QCP at P_c, and thus an unconventional pairing mechanism for the observed SC in MnP.

Similar to CrAs, the low-temperature normal-state resistivity of MnP near P_c also exhibits an nFL behavior $\rho(T) \propto T^n$ with $n \approx 1.5$, as seen in the inset of figure 26(a), consistent with the theoretical prediction for the incoherent scattering of quasi-particles near a 3D AF QCP [60, 61]. In addition, a dramatic enhancement of effective mass associated with the suppression of AF order was also evident from the significant enhancements of both the residual resistivity ρ_0 and the A coefficient near P_c (figures 26(b) and (c)), in which ρ_0 and A were obtained from a linear fitting to the $\rho(T^2)$ curves, i.e. $\rho = \rho_0 + AT^2$, in the low-temperature limit. These observations near P_c are regarded as characteristic signatures of an AF QCP in strongly correlated metallic systems, and provide important clues for the unconventional nature of the pressure-induced SC in MnP. Since the majority of the density of states

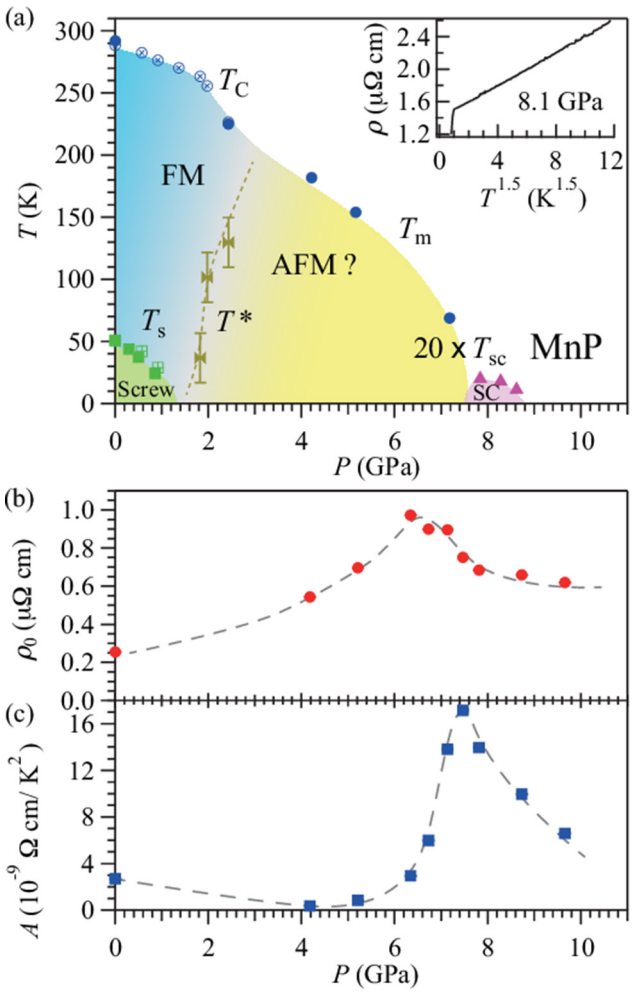

Figure 26. (a) Pressure dependences of the magnetic transition temperatures T_C, T_m, T^*, T_s, and the superconducting transition temperature T_c; T_c has been scaled by a factor of 20 for clarity. (b) and (c) Variation with pressure of the residual resistivity ρ_0 and the A coefficient extracted from a linear fitting to the $\rho(T^2)$ curves at the low-temperature limit. The inset of (a) shows the low-temperature resistivity data at 8.1 GPa in the form of ρ versus $T^{1.5}$. The relatively large error bar for T^* in (a) reflects the two-step feature evident in the ac magnetic susceptibility in figure 24(d). Reprinted figure with permission from [17], Copyright 2015 by the American Physical Society.

near the Fermi level for MnP is attributed to the Mn-3d states, our discovery makes MnP the first Mn-based superconductor, and the close proximity of SC to a magnetic instability suggests an unconventional pairing mechanism.

3.3. Follow-up investigations about the pressure-induced SC in MnP

At present, there are no experimental studies directly probing the superconducting properties of MnP, presumably due to the harsh conditions of $P \sim 8$ GPa and $T < 1$ K to achieve SC. The follow-up investigations on MnP are mainly dedicated to unveiling the nature of the new AF phase that is adjacent to the superconducting state, as shown in figure 26(a). So far, several techniques, including NMR [28], neutron diffraction [26], μSR [30], and x-ray magnetic diffraction [31] have been employed to study the nature of the AF state.

3.3.1. NMR. Fan *et al* employed the zero-field ^{31}P NMR at an ambient and hydrostatic pressure of 2 GPa to investigate the nature of the magnetic phases [28]. The conventional saturated recovery method was used to measure the ^{31}P NMR, having the RF oscillating field applied perpendicular to the *b* axis. The spectra were taken at the zero magnetic field by changing the transmitter frequency step-by-step and integrating the spin echo intensity. The magnitude of the RF pulse field has been taken as the parameter to determine whether MnP is in the helical state or not, i.e. a fairly low pulse level is needed to obtain the NMR signal in a helical state, whereas a much higher transmitter strength is required for the FM state and paramagnetic state.

Figure 27 displays the ^{31}P NMR spectra of MnP collected at various temperatures under ambient pressure and 2 GPa. At ambient pressure, the ^{31}P NMR spectra (figures 27(a) and (b)) in the helical state below 50 K can be obtained under a relatively low transmitter pulse level of 14, and are characterized by a broad, non-centrosymmetric line shape. In contrast, a transmitter pulse level as high as 250 has to be used to obtain the NMR spectra in the FM state (figures 27(c) and (d)) which features a rather narrow, symmetric peak. The change in temperature of the spectral line shape in the helical state has been attributed to the evolution of the helical character. Unfortunately, it is complicated to analyze the origin of the spectral line shape in that study. When the pressure was increased to 2 GPa, the ^{31}P NMR spectra in figures 27(e) and (f) were obtained under the transmitter pulse level of 18, which is very close to that used in the helical state at ambient pressure. The NMR signal from the helical phase can be observed even above 160 K. In addition, the resonance frequency range becomes wider in comparison with that of the ambient pressure, implying that the helical structure has a different character under high pressure. A similar temperature evolution of the helical structure to that at ambient pressure was also evident. Although the NMR study cannot elucidate the detailed helical structure, it demonstrated that the FM phase has been suppressed and a helical state different from that at ambient pressure takes place at 2 GPa.

3.3.2. Neutron diffraction. In order to determine the magnetic structure under high pressures, Matsuda *et al* recently performed NPD measurements on MnP single crystals grown with a modified Bridgeman method [26]. The pressure below and above 2 GPa was generated with a self-clamped piston-cylinder cell and a palm cubic anvil cell, respectively. The single crystal was mounted with (H, 0, L) in the horizontal scattering plane in the pressure cell. Figure 28(a) shows the temperature dependence of the (2, 0, 2) Bragg peak intensity at various pressures, which can be used as an order parameter for the FM transition. At ambient pressure, the (2, 0, 2) FM intensity develops below $T_C = 290$ K, and drops abruptly below $T_s \approx 40$ K when the helical-*c* structure develops with the magnetic peaks emerging at incommensurate positions that split along the L direction, such as the (2, 0, 2 $\pm\delta$) shown in figure 28(b). As seen in figure 28, both T_C and T_s decrease gradually with increasing pressure, and the incommensurability δ decreases slightly, suggesting that the FM

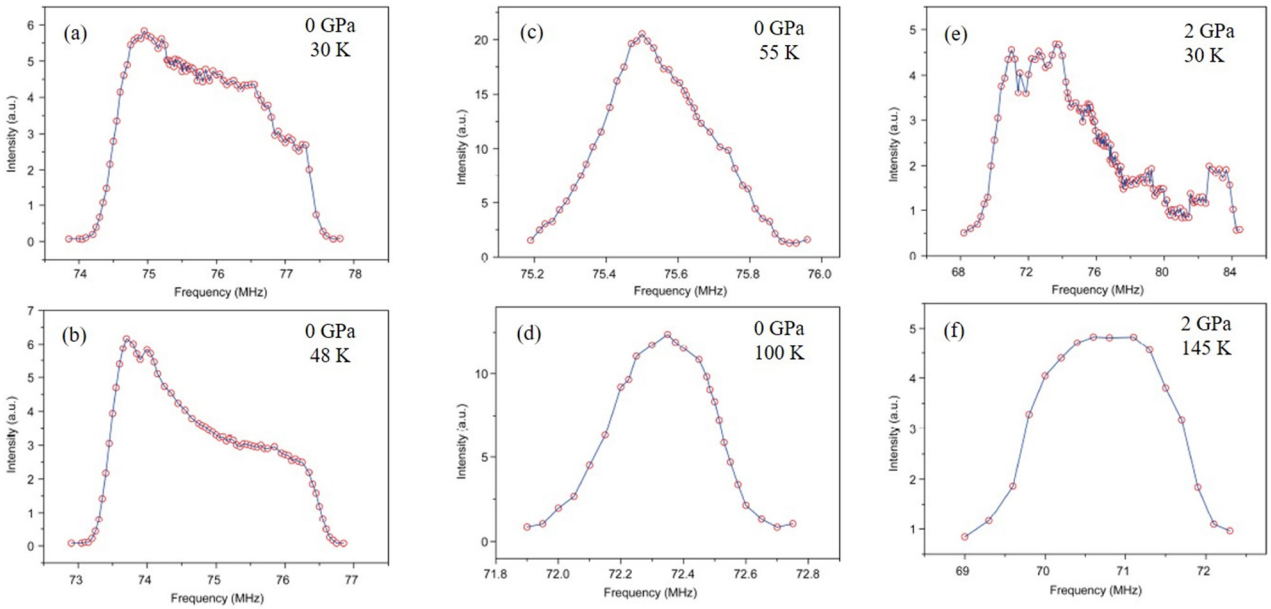

Figure 27. ^{31}P NMR spectra of the MnP single crystal. Under ambient pressure, for the helical phase at 30 K (a) and 48 K (b), a relatively low transmitter pulse field was used to detect the NMR signal; for the ferromagnetic phase at 55 K (c) and 100 K (d), a ten times higher transmitter pulse field was used to detect the NMR signal. Under a high pressure of 2 GPa, a much lower transmitter pulse field was used to detect the NMR signal in the helical state at 30 K (e) and 145 K (f). [28] 2016 © Science China Press and Springer-Verlag Berlin Heidelberg 2016. With permission of Springer.

interactions become dominant with pressure. At 1.1 GPa, the slight intensity drop of the (2, 0, 2) peak below 20 K and the very small intensity around (2, 0, 2.11) suggest that the FM phase becomes dominant and coexists with only a small fraction of the helical phase. T_C continues to decrease with pressure, and the temperature profile of the (2, 0, 2) peak changes for $P > 1.1$ GPa: the intensity becomes almost constant below 130 K at 1.6 GPa, and then a clear intensity reduction takes place around ~100 K at 1.8 GPa and ~140 K at 2 GPa. These characteristic temperatures are close to the T^* determined from the drop of ac magnetic susceptibility shown in figure 24(d). The magnetic intensity of the (2, 0, 2) peak decreases with pressure, indicating that the ferromagnetically ordered Mn moment is gradually reduced. At 165 K and 2 GPa, the magnetic ordered moment is estimated to be 0.7(1) μ_B, which is much reduced from the ordered moment of 1.3 μ_B at 60 K and ambient pressure.

Careful NPD experiments by Matsuda *et al* further revealed that the intensity drop of the (2, 0, 2) peak around T^* at 1.8 GPa is accompanied by the emergence of incommensurate peaks that split along the K direction, as shown in figures 29(a)–(c). From the intensity contour plot of figure 29(d), we can clearly see that the intensity at (2, $\pm\delta$, 2) and incommensurate δ gradually increases with a decrease in temperature. Interestingly, the development of the (2, $\pm\delta$, 2) incommensurate peaks can compensate the reduction of the (2, 0, 2) peak intensity, giving rise to a continuously increased total intensity (figure 29(e)) which strongly supports a magnetic origin for the observed incommensurate peak. Since the peak width is resolution limited, the magnetic phase below T^* should be a long-range ordered state. Based on a detailed structural symmetry analysis, Matsuda *et al* found that the observed incommensurate magnetic intensity can be best reproduced by a helical structure with the propagation vector $\boldsymbol{q}//b$ and the easy plane in the ac plane, which is denoted as the helical-b structure in order to distinguish the low-pressure helical-c structure, as shown in figure 30. Since the commensurate (2, 0, 2) peak remains below T^* in the intermediate pressure range, the actual magnetic structure can be described by either a two-phase model consisting of an FM and a helical-b structure, or a single-phase model with a conical structure, in which the b component is FM and the ac component is helical-b. Although the NPD experiments cannot distinguish between these two models, the gradual variations in temperature and pressure of δ and magnetic intensity are in favor of the conical model having the cone angle enlarged gradually with decreasing temperature and increasing pressure.

Upon a further increase in pressure to 3.8 GPa, the intensity of (2, 0, 2) reflection does not change with a decrease in temperature down to 3 K (figure 28(a)) suggesting that the FM order is completely suppressed. However, NPD experiments in the (0, H, L) scattering plane clearly show incommensurate magnetic peaks at (0, 1 $\pm\delta$, 1) below 208(5) K with $\delta = 0.141(1)$ r.l.u., as shown in figures 30(b) and (c). The magnetic structure thus becomes pure helical-b at this pressure, and the average magnetic moment is estimated to be 0.84 ± 0.14 μ_B at 5 K. Therefore, the conical or two-phase structure below T^* is considered to change continuously to a helical-b state below T_m. Interestingly, the incommensurability $\delta = 0.141$ at 3.8 GPa is very similar to that in CrAs ($\delta \sim 0.14$) at 0.88 GPa on the border of bulk SC. In addition, a similar pressure-induced spin reorientation from the ab to ac plane was also reported in CrAs in the vicinity of the superconducting phase [25].

3.3.3. μSR. Being a volume sensitive local magnetic probe, Khasanov *et al* also employed the μSR technique to investigate the pressure evolution of the magnetic orders in MnP [30]. They performed zero-field (ZF) and weak transverse field

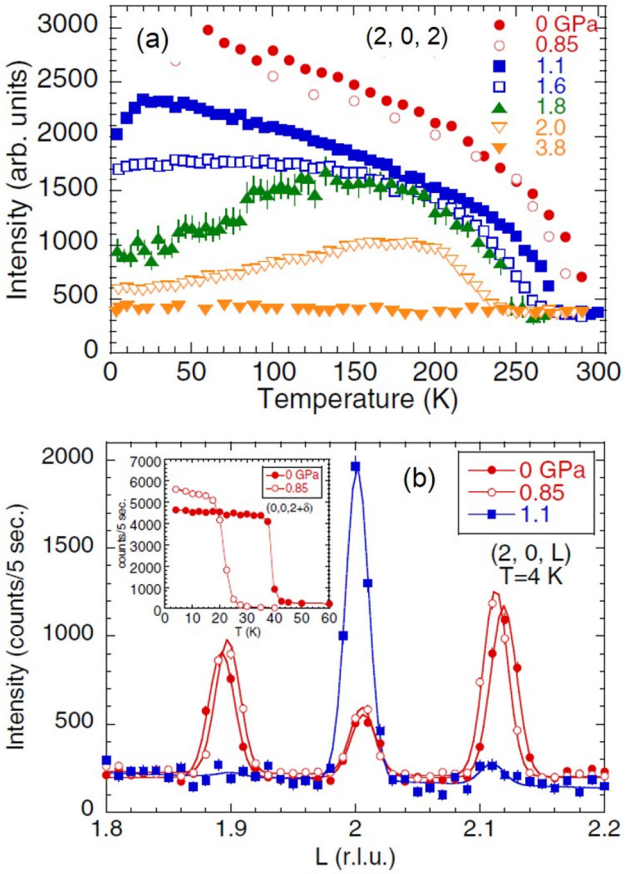

Figure 28. (a) Temperature dependence of the (2, 0, 2) Bragg intensity of MnP measured at various pressures. The finite intensity above T_C originates from nuclear Bragg intensity, which is used to normalize the data. (b) L scans around the (2, 0, 2) Bragg peak at 4 K as a function of pressure. r.l.u. stands for reciprocal lattice unit. The inset shows the temperature dependence of the incommensurate magnetic peak (0, 0, 2 $+\delta$) at 0 and 0.85 GPa. The solid lines are a guide to the eyes. Reprinted figure with permission from [26], Copyright 2016 by the American Physical Society.

(wTF) μSR experiments on polycrystalline MnP samples. In agreement with the above NPD studies, they also identified two kinds of incommensurate helical states with the propagation vector aligned along the c and b directions, respectively.

The ambient-pressure μSR results are shown in figures 31(a)–(c). The ZF–μSR asymmetry spectra $A(t)$ at $T < T_C$ (figure 31(a)) exhibit the spontaneous muon-spin precession, and the oscillatory part of $A(t)$ can be well fitted by an exponentially decaying cosine function with a zero initial phase, thus providing evidence of a commensurate magnetic order. The corresponding fast Fourier transform of the ZF–μSR data revealed a single sharp peak with a narrow internal field distribution (figure 31(g)). In contrast, the asymmetry spectra $A(t)$ in the helical-c state display a complicated oscillatory behavior (figure 31(c)) and its fast Fourier transform consists of a broad field distribution characterized by a minimum (B_{min}) and a maximum (B_{max}) cutoff field (figure 31(h)). These observations are in accordance with expectations for the double-helical incommensurate magnetic structure, which leads to a field distribution given by $P(B) = \frac{2}{\pi}\frac{B}{\sqrt{(B^2-B^2_{min})(B^2_{max}-B^2)}}$, characterized by two peaks at a minimum B_{min} and a maximum B_{max} cutoff field. Both B_{min} and B_{max} were found to abruptly drop to zero at T_s, indicating the first-order character of the transition. In a broad temperature range 30 K $\leqslant T \leqslant$ 50 K both orders are detected simultaneously (figure 31(b)).

Displayed in figures 31(d)–(f) are the ZF–μSR results at $P = 2.42$ GPa when the FM order has been suppressed to $T_C = 250$ K. Similarly, a spontaneous muon-spin precession can be observed in the asymmetry spectra $A(t)$ of the FM state at 200 K (figure 31(d)). Upon further decreasing the temperature to 100 K and 5 K, the asymmetry spectra $A(t)$ are characterized by a higher internal field, and the oscillatory part can be described by the Gaussian decaying cosine function with zero initial phase (figures 31(e) and (f)). As shown in figure 31(i), the fast Fourier transform revealed a single, symmetric but broad internal magnetic field distribution $P(B)$, which at first glance seems to be inconsistent with a helical order. Khasanov *et al* pointed out that under certain conditions the sum of four asymmetric $P(B)$ distributions for a helical-b magnetic order can result in a single broad symmetric line as observed [30], but the exact spin arrangement of the helical-b structure cannot be resolved from the μSR experiments. Similar to the ambient pressure, the transition from FM to the helical-b state is first order in nature, resulting in a broad two-phase coexistent temperature range at 2.42 GPa. Thus, both the neutron and μSR experiments are in favor of the helical-b structure under high pressures.

3.3.4. Synchrotron x-ray magnetic diffraction. Wang *et al* also investigated the evolution of magnetic phases under pressure by utilizing a synchrotron-based non-resonant x-ray magnetic diffraction technique [31]. MnP single crystals grown with the Sn-flux method were pressurized with a diamond anvil cell filled with liquid PTM. Although a helical order was also evident for the high-pressure AF phase, the propagation vector **q** was found to remain along the orthorhombic c axis with a shorter periodicity.

Their major experimental results are shown in figure 32, which depicts the XRDs of MnP single crystal under various pressures at 4 K. As shown in figure 32(a), a pair of non-resonant magnetic peaks can be clearly observed at (1, 0, 1 $\pm\delta$), which are associated with the helical spin order (Hc-I) with $\delta \sim$ (0, 0, 0.117) at ambient pressure. Upon increasing pressure, a pair of superlattice peaks in mirror symmetry to the lattice Bragg reflection are still observable at (0, 0, 1 $\pm\delta$) with $\delta \approx 0.25$ for $P = 3.17$, 5.28, and 6.43 GPa (figures 32(b)–(d)), but they are absent for $P = 8.99$ GPa (figure 32(e)). The authors have ascribed the observed new superlattice peaks to a new helical order with tightened pitch, i.e. Hc-II. In this case, the propagation vector **q** remains along the c axis, but the periodicity of spiral spins becomes about half of the Hc-I order. Therefore, the magnetic XRD provided a different solution for the new AF structure at high pressure in comparison with the above neutron [26] and μSR [30] studies. As noted by Wang *et al* [31], the limited number of observed diffraction peaks and the lack of a full azimuthal study due to constrained

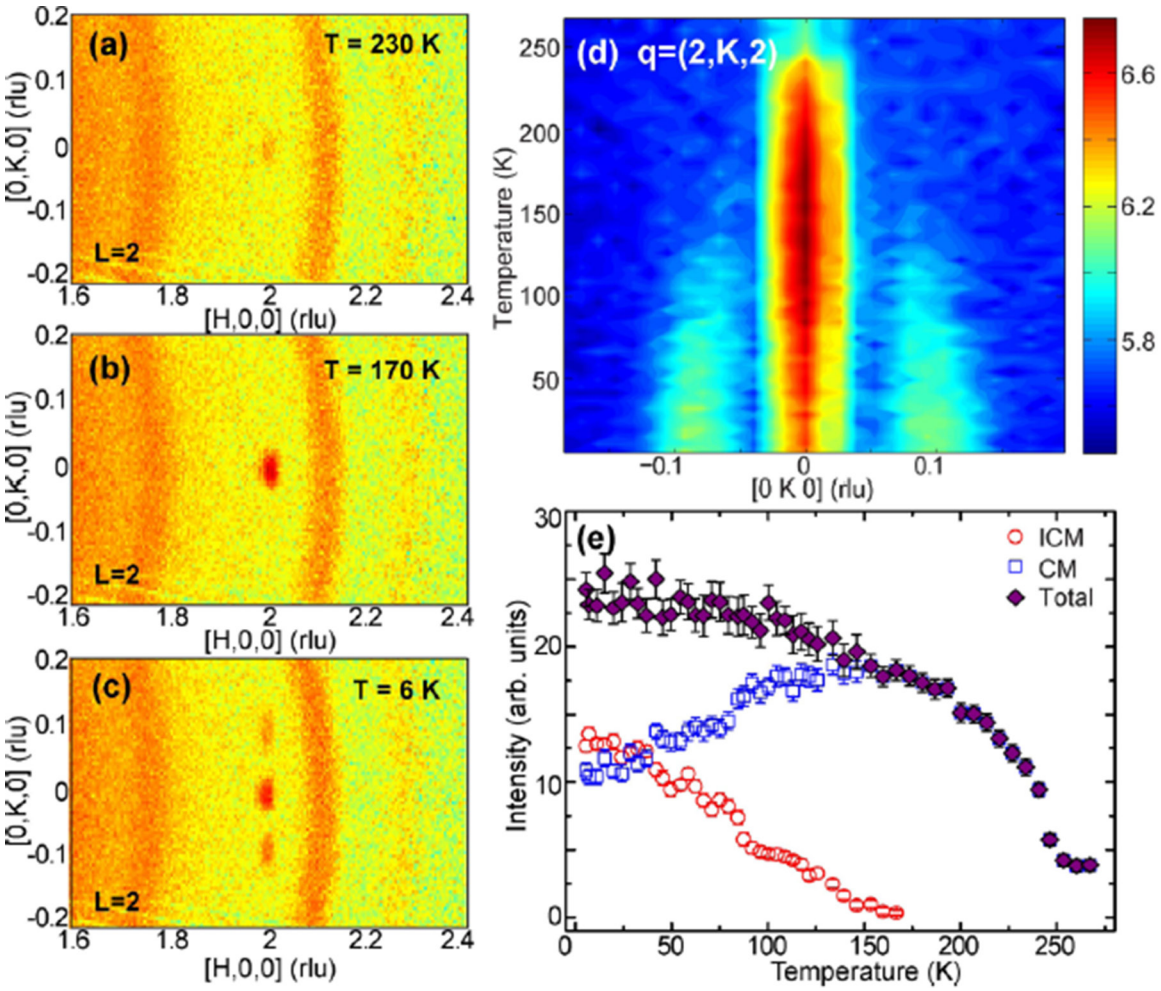

Figure 29. Intensity contour plot of NPD at 1.8 GPa in the (H, K, 2) scattering plane measured at (a) 230 K, (b) 170 K and (c) 6 K for MnP. The arc-shaped signals are powder lines from the Zr-based amorphous pressure cell. (d) Intensity contour plot of the (2, K, 2) ($-0.2 \leqslant K \leqslant 0.2$ r.l.u.) intensities as a function of temperature. (e) Temperature dependence of the (2, 0, 2) commensurate intensity, sum of the (2, $\pm\delta$, 2) incommensurate magnetic intensities, and the total intensity at 1.8 GPa. Reprinted figure with permission from [26], Copyright 2016 by the American Physical Society.

high-pressure cell geometry made it insufficient to fully refine the spin structure at higher pressures. Another issue that deserves careful scrutiny is the influence of the sample's purity on the different magnetic structure. These discrepancies regarding the high-pressure magnetic structure of MnP call for further studies, in particular the high-pressure NPD on the flux-grown MnP crystals.

3.3.5. Theoretical investigations. In order to assess the magnetic state of MnP under high pressure, Bonfà *et al* performed an *ab initio* study with density functional theory simulations [33]. Their calculations can reproduce the low-temperature helical-c and the FM state ambient pressure, and further confirmed the helical-b as the magnetic ground state that precedes the superconducting state in figure 26(a). Chong *et al* recently investigated the electronic structure and superconducting properties of MnX (X = N, P, As, Sb) under high pressures [92]. They found a sharp increase in the superconducting critical temperature T_c of MnP near the critical pressure $P_c \sim 8$ GPa, which is attributed to an enhancement of the electron–phonon coupling constant and the electronic density of states at the Fermi level. They pointed out that the T_c of MnAs and MnSb is higher than MnP, implying that MnAs and MnSb may demonstrate greater potential for Mn-based superconducting materials. Whether the observed SC in MnP is a conventional BCS type or an unconventional one deserves further investigation.

4. Perspectives and concluding remarks

In summary, we gave a brief review of the recent progress regarding the pressure-induced SC in CrAs and MnP. These two compounds belong to a large family of transition-metal monopnictides that have been extensively investigated since the 1960s due to the observations of interesting structural and magnetic properties. In particular, both CrAs and MnP crystallize in the orthorhombically distorted NiAs-type structure and adopt the double helical magnetic ground state characterized by distinct propagation vectors $\mathbf{q} = 0.354 \times 2\pi c^*$ and $0.117 \times 2\pi c^*$, which correspond to dominant AF and FM nearest-neighbor exchange interactions, respectively. For CrAs, the HM order at $T_N = 270$ K is a strong first order transition accompanied by drastic structural responses, whose origin remains poorly understood. Yet the coupled magnetic and structural transitions

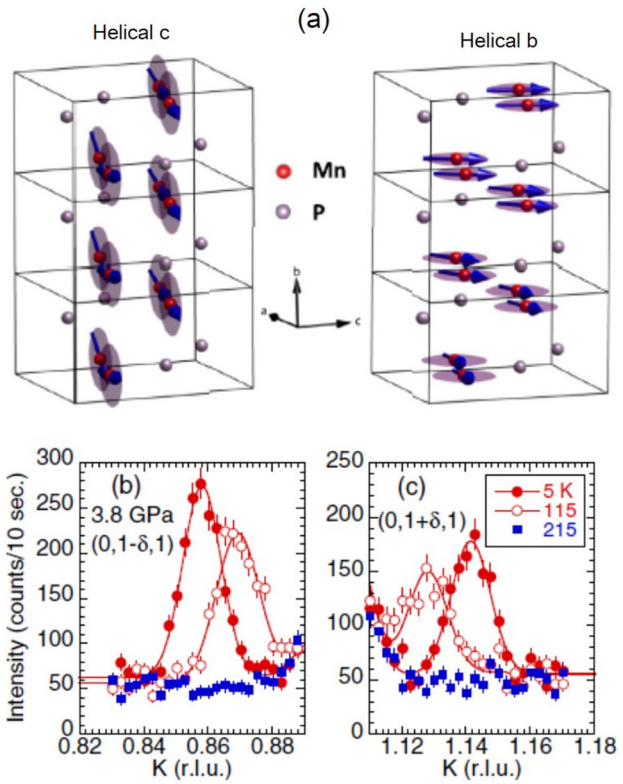

Figure 30. (a) Helical spin structures under low pressure (helical *c*) and high pressure (helical *b*) for MnP. (b) and (c) The incommensurate magnetic peaks at (0, 1 $\pm\delta$, 1) observed at 3.8 GPa and different temperatures. The solid lines are a guide to the eye. Reprinted figure with permission from [26], Copyright 2016 by the American Physical Society.

are prone to suppression via either chemical substitutions or applying physical pressure. On the other hand, a ferromagnetic order first takes place at $T_C = 290$ K prior to the helimagnetic transition at $T_s = 50$ K for MnP, in which the strong magnetic anisotropy and the metamagnetism give rise to rich magnetic phase diagrams containing a variety of magnetically ordered states for *H*//*a* or *H*//*c*. Both compounds are confirmed to be correlated Fermi-liquid metals and exhibit characteristic resistivity anomalies at their magnetic transitions.

When CrAs is subjected to high pressure, its first-order helimagnetic transition can be readily suppressed and disappears completely around $P_c \approx 0.8$ GPa; bulk SC with an optimal $T_c \approx 2$ K emerges near P_c and displays a dome-shaped $T_c(P)$, reminiscent of many unconventional superconducting systems. The helimagnetic transition remains first order until P_c, resulting in a two-phase coexistent region for ~0.35 GPa $< P < P_c$. NQR measurements under pressure reveal no evidence of the coherence effect near T_c and a T^3 dependence of $1/T_1$ below T_c, which are in favor of the unconventional mechanism for the observed SC with line nodes in the superconducting gap function. The observations of nFL behavior and a dramatic enhancement of the effective mass near P_c, which are characteristics of AF QCP, signal the important role of critical spin fluctuations for the transport properties of CrAs. In addition, experimental results from NMR and neutron scattering under pressure also indicate the importance of magnetism and its possible interplay with the observed SC.

When MnP is subjected to high pressure, its magnetic states undergo intriguing evolutions: the ambient-pressure helimagnetic order with $T_s = 50$ K disappears completely around 1.2 GPa; another new AF phase emerges above 1.5 GPa and its transition temperature T^* rises quickly and merges with the declining FM transition around 3 GPa, above which the magnetic ground state becomes the new AF phase. Subsequent measurements of NMR, NPD, and magnetic XRD confirmed that the new AF phase also takes the double helical order, yet likely having different propagation vectors compared to the ambient-pressure helimagnetic phase. This new AF phase is eventually suppressed around $P_c \approx 8$ GPa, where SC with a maximum $T_c \approx 1$ K appears within a narrow pressure range of ~1 GPa. Similar to the CrAs case, characteristic behaviors of AF QCP were also observed near P_c, implying the possible magnetic-mediated SC in MnP.

There are a number of open issues to be addressed in the future regarding the peculiar normal-state magnetic and superconducting properties:

4.1. The helical order and its evolution under pressure

As mentioned above, the origin of the first-order helimagnetic transition and its intimate correlation with the dramatic structure changes in CrAs remains poorly understood and calls for future in-depth experimental and theoretical investigations. The difficulty with this problem might have a deep root in the correct description of the electronic states of Cr-3d electrons which should lie in the crossover regime of localized-to-itinerant electron transition. On the other hand, what is the key factor governing the FM to the helimagnetic transition in MnP? It is generally thought that the competition between FM and AF interactions is essential for the helimagnetic order. How does the thermal contraction of the orthorhombic lattice influence the competition?

On the other hand, the helimagnetic orders in both compounds have been reported to undergo a spin reorientation under pressure from the *ab* to the *ac* plane, which, however, was not supported by other experiments, such as the synchrotron x-ray magnetic diffraction measurements [31]. Future investigations are thus needed to resolve these discrepancies, which might be affected sensitively by the pressure homogeneity and/or the sample purity. If the pressure-induced spin reorientation is true, then what is the driving force and the common origin for both compounds?

4.2. Conventional versus unconventional SC

As mentioned above, the close proximity of SC to the helimagnetic order in the phase diagram and the absence of a coherent effect near the T_c of CrAs point to the unconventional nature of the observed SC. However, the temperature dependence of superfluid density based on the penetration depth measurements suggests a conventional BCS SC. In addition, the strong first-order nature of the helimagnetic transition up to P_c makes the argument of magnetic quantum criticality a bit elusive. But it should be noted that the SC in CrAs is very sensitive to sample purity and disorders; the penetration depth measurements

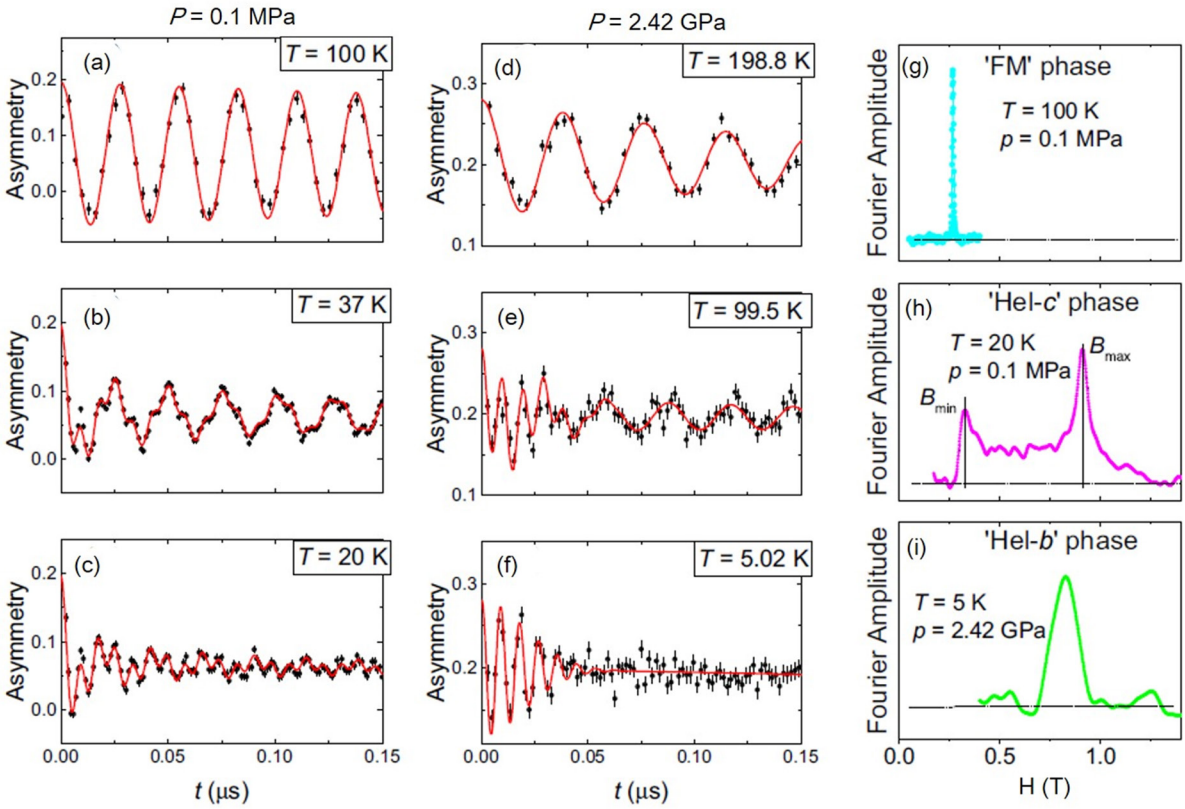

Figure 31. (a)–(c) Ambient-pressure ZF–μSR asymmetry spectra of MnP at $T = 100$ K (FM phase), $T = 37$ K (mixture of FM and helical-*c* phases), and $T = 20$ K (helical-*c* phase); (e) and (f) ZF–μSR asymmetry spectra at 2.42 GPa for $T = 198.8$ K (FM phase), $T = 99.5$ K (mixture of FM and helical-*b* phases), and $T = 5.02$ K (helical-*b* phase); (h) and (i) the magnetic field distribution (fast Fourier transform of the ZF–μSR data) in the FM, helical-*c* and helical-*b* state, respectively. Reprinted figure with permission from [30], Copyright 2016 by the American Physical Society.

were performed on the polycrystalline CrAs samples in which the presence of bulk SC with optimal T_c was not reported. In addition, the temperature dependence of the spin-relaxation rate $1/T_1$ was measured down to 0.7 K, ~$0.3T_c$, which is generally insufficient to obtain reliable information about the superconducting gap symmetry; instead, measurements down to 100 mK (~$T_c/20$) or below are needed. Therefore, comprehensive NMR and μSR investigations on high-quality single crystals in a large temperature range are highly desirable in order to correctly describe the nature of the superconducting state.

Due to the harsh experimental conditions for realizing the SC in MnP, the properties of its superconducting state remain largely uncharacterized to date. In this case, the high-quality single crystals are easily available; the major obstacles come from the experimental techniques, such as high-pressure NMR [93] and μSR, which should be performed up to 8 GPa and well below 1 K.

4.3. Relationship of helimagnetism and SC

As pointed out by Norman [37], the SC in both CrAs and MnP occur on the border of helimagnetic order, which is rare since collinear AF orders are commonly seen in the known unconventional superconducting systems. If the magnetism-mediated mechanism is important, what is the special role of the helimagnetic fluctuations for the observed SC? Wang *et al* [31] have argued that the periodicity of the helimagnetic order is an important factor for mediating the Cooper pairs, and the great tunability of the pitch of helical order among the transition-metal monopnictides provides an effective means for searching more superconductors near the helimagnetic QCP. FeP and FeAs have a similar MnP-type crystal structure and also adopt the double helical magnetic order as CrAs and MnP. Therefore, it is interesting to explore whether SC can be achieved in the vicinity of the helimagnetic QCP of FeP and FeAs.

4.4. More Cr- and Mn-based superconductors

Since the electronic density of states at the Fermi energy are dominated by 3d-electrons, CrAs and MnP are respectively the first superconductor among the Cr- and Mn-based compounds which are commonly believed to be antagonistic to SC. These discoveries thus opened a new avenue to search for novel superconductors among the Cr- and Mn-based compounds. One of the exciting recent achievements in this direction is the discovery of SC in the quasi-1D $A_2Cr_3As_3$ (A = K, Rb, Cs) by Cao's group in Zhejiang University. Is it possible to discover more Cr- and Mn-based superconductors, especially with a higher T_c? To this end, the application of chemical pressure via the substitution of As with P in $CrAs_{1-x}P_x$ seems to be a plausible way in analogue to the high pressure. Unfortunately, preliminary experimental attempts are negative, presumably due to the great sensitivity of SC to the disorders that are unavoidable in these chemically substituted

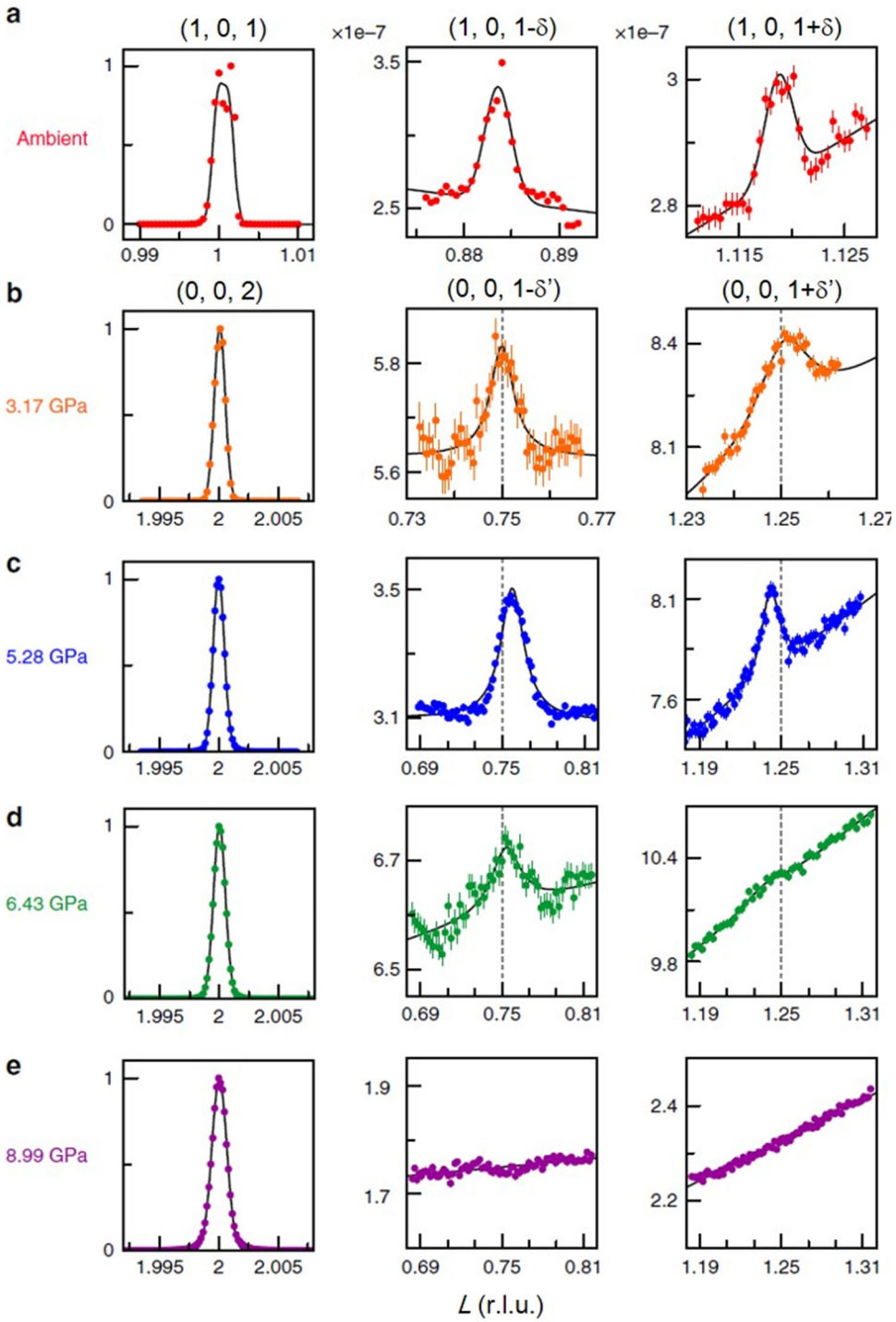

Figure 32. X-ray diffraction evidence of helical order in MnP. (a) Raw scans around (1, 0, 1) order at ambient pressure and $T = 4$ K, showing both the lattice Bragg peak and a pair of non-resonant magnetic peaks (1, 0, 1 $\pm\delta$) associated with the helical order $\delta = 0.117$ r.l.u. Solid lines are a guide to eye. (b)–(d) Longitudinal line shapes of (0, 0, 2) lattice and (0, 0, 1 $\pm\delta'$) helical magnetic order with $\delta' \approx 0.25$ r.l.u. measured at $T = 4$ K under various pressures. (e) At 8.99 GPa, the magnetic diffraction is no longer observed in longitudinal scans at the same positions of (b)–(d). Reproduced from [31]. CC BY 4.0.

samples. On the other hand, the preparation of $MnP_{1-x}N_x$ is also challenging. Alternatively, it is instructive to explore more Cr- and Mn-based systems with different types of crystal structures. Based on previous experience, low-dimensional systems might favor a higher T_c. Apparently, the combination of material design and effective chemical synthesis routes will be helpful to find more Cr- and Mn-based superconductors.

Acknowledgments

The authors acknowledge the support from the National Natural Science Foundation of China (Grant No. 11574377, 11674375, 11634015), the National Basic Research Program of China (Grant Nos. 2014CB921500, 2015CB921300), the Strategic Priority Research Program and the Key

Research Program of Frontier Sciences of the Chinese Academy of Sciences (Grant Nos. XDB07020000 and QYZDB-SSW-SLH013).

References

[1] Norman M R 2011 *Science* **332** 196
[2] Steglich F, Aarts J, Bredl C D, Lieke W, Meschede D and Franz W 1979 *Phys. Rev. Lett.* **43** 1892
[3] Bednorz J G and Muller K A 1986 *Z. Phys.* B **64** 189
[4] Kamihara Y, Watanabe T, Hirano M and Hosono H 2008 *J. Am. Chem. Soc.* **130** 3296
[5] Canfield P C 2011 *Nat. Mater.* **10** 259
[6] Ni N, Tillman M E, Yan J-Q, Kracher A, Hannahs S T, Bud'ko S L and Canfield P C 2008 *Phys. Rev.* B **78** 214515
[7] Sefat A S, Singh D J, VanBebber L H, Mozharivskyj Y, McGuire M A, JIn R, Sales B C, Keppens V and Mandrus D 2009 *Phys. Rev.* B **79** 224524
[8] Cheng P, Shen B, Hu J P and Wen H H 2010 *Phys. Rev.* B **81** 174529
[9] Simonson J W *et al* 2012 *Proc. Natl Acad. Sci. USA* **109** E1815
[10] Guo J *et al* 2013 *Sci. Rep.* **3** 2555
[11] Mathur N D, Grosche F M, Julian S R, Walker I R, Freye D M, Haselwimmer R K W and Lonzarich G G 1998 *Nature* **394** 39
[12] Monthoux P, Pines D and Lonzarich G G 2007 *Nature* **450** 1177
[13] Dai P, Hu J and Dagotto E 2012 *Nat. Phys.* **8** 709
[14] Gegenwart P, Si Q and Steglich F 2008 *Nat. Phys.* **4** 186
[15] Kasahara S *et al* 2010 *Phys. Rev.* B **81** 184519
[16] Wu W, Cheng J-G, Matsubayashi K, Kong P P, Lin F K, Jin C Q, Wang N L, Uwatoko Y and Luo J L 2014 *Nat. Commun.* **5** 5508
[17] Cheng J-G, Matsubayashi K, Wu W, Sun J P, Lin F K, Luo J L and Uwatoko Y 2015 *Phys. Rev. Lett.* **114** 117001
[18] Selte K, Kjekshus A, Jamison W E, Andresen A F and Engebretsen J E 1971 *Acta Chem. Scand.* **25** 1703
[19] Boller H and Kallel A 1971 *Solid State Commun.* **9** 1699
[20] Huber E E J and Ridgley H D 1963 *J. Appl. Phys.* **34** 1099
[21] Huber E E J and Ridgley H D 1964 *Phys. Rev.* **135** A1033
[22] Forsyth J B, Pickart S J and Brown P J 1966 *Proc. Phys. Soc.* **88** 333
[23] Felcher G P 1966 *J. Appl. Phys.* **37** 1056
[24] Keller L, White J S, Frontzek M, Babkevich P, Susner M A, Sims Z C, Sefat A S, Ronnow H M and Ruegg C 2015 *Phys. Rev.* B **91** 020409
[25] Shen Y *et al* 2016 *Phys. Rev.* B **93** 060503
[26] Matsuda M *et al* 2016 *Phys. Rev.* B **93** 100405
[27] Kotegawa H, Nakahara S, Akamatsu R, Tou H, Sugawara H and Harima H 2015 *Phys. Rev. Lett.* **114** 117002
[28] Fan G Z, Zhao B, Wu W, Zheng P and Luo J L 2016 *Sci. China Phys. Mech. Astron.* **59** 657403
[29] Khasanov R *et al* 2015 *Sci. Rep.* **5** 13788
[30] Khasanov R, Amato A, Bonfa P, Guguchia Z, Luetkens H, Morenzoni E, De Renzi R and Zhigadlo N D 2016 *Phys. Rev.* B **93** 180509
[31] Wang Y S, Feng Y J, Cheng J-G, Wu W, Luo J L and Rosenbaum T F 2016 *Nat. Commun.* **7** 13037
[32] Zheng P, Xu Y J, Wu W, Xu G, Lv J L, Lin F K, Wang P, Yang Y F and Luo J L 2016 in preparation (arXiv: 1607.02853v1)
[33] Bonfa P, Onuorah I J and De Renzi R 2016 in preparation (arXiv: 1603.08891v1)
[34] Mackenzie A P, Haselwimmer R K W, Tyler A W, Lonzarich G G, Mori Y, Nishizaki S and Maeno Y 1998 *Phys. Rev. Lett.* **80** 161
[35] Saxena S S *et al* 2000 *Nature* **406** 587
[36] Kotegawa H, Nakahara S, Tou H and Sugawara H 2014 *J. Phys. Soc. Japan* **83** 093702
[37] Norman M R 2015 *Physics* **8** 24
[38] Bao J-K *et al* 2015 *Phys. Rev.* X **5** 011013
[39] Tang Z-T *et al* 2015 *Phys. Rev.* B **91** 020506
[40] Tang Z-T *et al* 2015 *Sci. China Mater.* **58** 16
[41] Motizuki K, Ido H, Itoh T and Morifuji M 2009 Electronic structure and magnetism of 3D-transition-metal pnictides *Springer Series in Materials Science* vol 131, ed R Hull *et al* (Berlin: Springer)
[42] Ido H 1987 *J. Magn. Magn. Mater.* **70** 205
[43] Watanabe H, Kazama N, Yamaguchi Y and Ohashi M 1969 *J. Appl. Phys.* **40** 1128
[44] Kanaya K, Abe S, Yoshida H, Kamigaki K and Kaneko T 2004 *J. Alloys Compd.* **383** 189
[45] Kazama N and Watanabe H 1971 *J. Phys. Soc. Japan* **30** 1319
[46] Zhang G M, Su Y H, Lu Z Y, Weng Z Y, Lee D H and Xiang T 2009 *Europhys. Lett.* **86** 37006
[47] Wu W, Zhang X D, Yin Z H, Zheng P, Wang N L and Luo J L 2010 *Sci. China* **53** 1207
[48] Kazama N and Watanabe H 1971 *J. Phys. Soc. Japan* **31** 943
[49] Barner K, Santandrea C, Neitzel U and Gmelin E 1984 *Phys. Status Solidi* b **123** 541
[50] Suzuki T and Ido H 1993 *J. Appl. Phys.* **73** 5686
[51] Selte K, Kjekshus A, Peterzens P G and Andresen A F 1978 *Acta Chem. Scand.* **A32** 653
[52] Fjellavg H, Kjekshus A, Stolen S and Andresen A F 1988 *Acta Chem. Scand.* **A42** 214
[53] Selte K, Hjersing H, Kjekshus A, Andresen A F and Fischer P 1975 *Acta Chem. Scand.* A **29** 695
[54] Suzuki T and Ido H 1986 *J. Magn. Magn. Mater.* **54–7** 935
[55] Zavadskii E A and Sibarova I A 1980 *Sov. Phys—JETP* **51** 542
[56] Yoshida H, Kaneko T, Shono M, Abe S and Ohashi M 1980 *J. Magn. Magn. Mater.* **15–8** 1147
[57] Okada T, Ogino H, Yakita H, Yamamoto A, Kishio K and Shimoyama J 2014 *Physica* C **505** 1
[58] Jin K, Butch N P, Kirshenbaum K, Paglione J and Greene R L 2011 *Nature* **476** 73
[59] Paglione J and Greedan J E 2010 *Nat. Phys.* **6** 645
[60] Moriya T 1985 *Spin Fluctuations in Itinerant Electron Magnetism* (Berlin: Springer)
[61] Moriya T and Takimoto T 1995 *J. Phys. Soc. Japan* **64** 960
[62] Yu Z H *et al* 2015 *Proc. Natl. Acad. Sci. USA* **112** 14766
[63] Imai T, Ahilan K, Ning F L, McQueen T M and Cava R J 2009 *Phys. Rev. Lett.* **102** 177005
[64] Kitagawa K, Katayama N, Gotou H, Yagi T, Ohgushi K, Matsumoto T, Uwatoko Y and Takigawa M 2009 *Phys. Rev. Lett.* **103** 257002
[65] Zhu X D, Ling L S, Han Y Y, Xu J M, Wang Y J, Zhang H W, Zhang C J, Pi L and Zhang Y H 2016 *J. Alloys Compd.* **677** 57
[66] Niu Q *et al* 2017 *Nat. Commun.* **8** 15358
[67] Wihitmore B G 1929 *Phil. Mag.* **7** 125
[68] Bates L F 1929 *Phil. Mag.* **8** 714
[69] Goodenough J B 1964 *J. Appl. Phys.* **35** 1083
[70] Moon R M 1982 *J. Appl. Phys.* **53** 1956
[71] Komatsubara T, Kinoshita K and Hirahara E 1956 *J. Phys. Soc. Japan* **20** 2036
[72] Stein B F and Walmsley R H 1966 *Phys. Rev.* **148** 933
[73] Komatsubara T, Shinohara S, Suzuki T and Hirahara E 1969 *J. Appl. Phys.* **40** 1037
[74] Komatsubara T, Suzuki T and Hirahara E 1970 *J. Phys. Soc. Japan* **28** 317
[75] Ishizaki A, Komatsubara T and Hirahara E 1971 *J. Phys. Soc. Japan* **30** 292
[76] Becerra C C, Shapira Y, Oliveira J N F and Chang T S 1980 *Phys. Rev. Lett.* **44** 1692

[77] Shapira Y, Becerra C C, Oliveira J N F and Chang T S 1981 *Phys. Rev.* B **24** 2780
[78] Yoshizawa H, Shapiro S M and Komatsubara T 1985 *J. Phys. Soc. Japan* **54** 3084
[79] Bindilatti V, Becerra C C and Oliveira J N F 1989 *Phys. Rev.* B **40** 9412
[80] Becerra C C, Bindilatti V and Oliveira J N F 2000 *Phys. Rev.* B **62** 8965
[81] Zieba A, Becerra C C, Fjellvag H, Oliveira J N F and Kjekshus A 1992 *Phys. Rev.* B **46** 3380
[82] Reis M S *et al* 2008 *Phys. Rev.* B **77** 104439
[83] Suzuki T, Matsumura Y and Hirahara E 1966 *J. Phys. Soc. Japan* **21** 1621
[84] Takase A and Kasuya T 1980 *J. Phys. Soc. Japan* **48** 430
[85] Takase A, Yashima H and Kasuya T 1979 *J. Phys. Soc. Japan* **47** 531
[86] Yanase A and Hasegawa A 1980 *J. Phys. C: Solid State Phys.* **13** 1989
[87] Perkins P G, Marwaha A K and Stewart J J P 1981 *Theor. Chim. Acta* **59** 569
[88] Hirahara E, Suzuki T and Matsumura Y 1968 *J. Appl. Phys.* **39** 713
[89] Kamigaich T, Okamoto T, Iwata N and Tatsumoto E 1968 *J. Phys. Soc. Japan* **24** 649
[90] Grazhdankina N P, Burkhanov A M and Bersenev Y S 1969 *Sov. Phys—JETP* **28** 1141
[91] Banus M D 1972 *J. Solid State Chem.* **4** 391
[92] Chong X Y, Jiang Y H, Zhou R and Feng J 2016 *Sci. Rep.* **6** 21821
[93] Fukazawa H, Yamatoji N, Kohori Y, Terakura C, Takeshita N, Tokura Y and Takagi H 2007 *Rev. Sci. Instrum.* **78** 015106